

Winter 1994

Wind-driven observation and modelling in the Strait of Gibraltar

Benabdeljelil Abdelkader
University of New Hampshire, Durham

Follow this and additional works at: <https://scholars.unh.edu/dissertation>

Recommended Citation

Abdelkader, Benabdeljelil, "Wind-driven observation and modelling in the Strait of Gibraltar" (1994). *Doctoral Dissertations*. 1813.
<https://scholars.unh.edu/dissertation/1813>

This Dissertation is brought to you for free and open access by the Student Scholarship at University of New Hampshire Scholars' Repository. It has been accepted for inclusion in Doctoral Dissertations by an authorized administrator of University of New Hampshire Scholars' Repository. For more information, please contact nicole.hentz@unh.edu.

INFORMATION TO USERS

This manuscript has been reproduced from the microfilm master. UMI films the text directly from the original or copy submitted. Thus, some thesis and dissertation copies are in typewriter face, while others may be from any type of computer printer.

The quality of this reproduction is dependent upon the quality of the copy submitted. Broken or indistinct print, colored or poor quality illustrations and photographs, print bleedthrough, substandard margins, and improper alignment can adversely affect reproduction.

In the unlikely event that the author did not send UMI a complete manuscript and there are missing pages, these will be noted. Also, if unauthorized copyright material had to be removed, a note will indicate the deletion.

Oversize materials (e.g., maps, drawings, charts) are reproduced by sectioning the original, beginning at the upper left-hand corner and continuing from left to right in equal sections with small overlaps. Each original is also photographed in one exposure and is included in reduced form at the back of the book.

Photographs included in the original manuscript have been reproduced xerographically in this copy. Higher quality 6" x 9" black and white photographic prints are available for any photographs or illustrations appearing in this copy for an additional charge. Contact UMI directly to order.

UMI

University Microfilms International
A Bell & Howell Information Company
300 North Zeeb Road, Ann Arbor, MI 48106-1346 USA
313/761-4700 800/521-0600

Order Number 9518478

**Wind-driven observation and modelling in the Strait of
Gibraltar**

Abdelkader, Benabdeljelil, Ph.D.

University of New Hampshire, 1994

U·M·I
300 N. Zeeb Rd.
Ann Arbor, MI 48106

WIND-DRIVEN OBSERVATION AND MODELLING IN
THE STRAIT OF GIBRALTAR

BY

Abdelkader Benabdeljelil
Doctorat 3ème Cycle, Université Louis Pasteur
Strasbourg-France, 1984

DISSERTATION

Submitted to the University of New Hampshire
in Partial Fulfillment of
the Requirements for the Degree of

Doctor of Philosophy

in

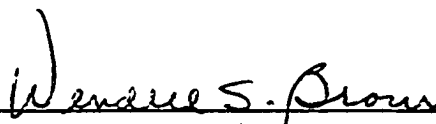
Earth Sciences: Oceanography

December, 1994

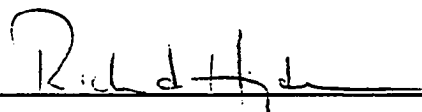
This dissertation has been examined and approved.



Dissertation director, Neal R. Pettigrew
Associate Professor of Oceanography,
University of Maine
Adjunct Professor of Earth Sciences,
University of New Hampshire



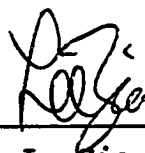
Wendell S. Brown
Professor of Earth Sciences and Earth, Oceans and Space,
University of New Hampshire



Richard A. Hyde
Associate Professor of Physics,
Norwich University



James D. Irish
Research Specialist,
Woods Hole Oceanographic Institution



Lee L. Zia
Associate Professor of Mathematics,
University of New Hampshire

November 3, 1994

Date

In memory of my Father
May his Blessings be Eternal

To my Mother
for Love that never failed

To Lalla Aïcha and Kelthoum
My Twin Pillars in life

ACKNOWLEDGEMENTS

I would like to express my deepest gratitude to my thesis advisor Dr. Pettigrew for his constant support and patience. He accepted to direct this work with kindness and a great deal of tolerance. From him I have learned, among other things, that Oceanography is the physics behind the crude and tempting mathematics. This work is undoubtedly the result of his consistent encouragements and his calming influence throughout the last eight years. His friendship made my life a lot easier.

I would like to thank Dr Hyde for convincing me that numerical analysis could bring some insight to physical problems and for building the core of the computer program.

I would sincerely like to thank all the members of my doctoral committee for their editorial remarks, criticism and support.

I am grateful to Dean Richards of the University of New Hampshire who always believed in me and provided my wife and me more support than we would have imagined.

I owe a great deal to OPAL-UNH, as a team and to each one, for providing cheerful friendship and sturdy advice, both in my research and my social life. May Mel L.C. (the warmest and most caring hugs of all), Karen G. (the real computer woman), Russ G. (no program could trick him), Frank

O.S. (the best jokes in town), and all my fellow graduate students find here my sincere appreciation for their friendship and unselfish caring.

I owe a special debt of gratitude to the Department of Oceanography of the University of Maine. Each faculty, staff and student member made me feel part of the team. I will miss each one of them.

Finally, very special thanks are due to John Wallinga, who provided me generously with housing during the last months of my stay in Maine. I will always cherish the late evening floats and good British comedy.

My wife, Dr Lalla Aïcha Lamrani should be awarded a special decoration for putting up with me and holding our family together and keeping us happy during all these years. Special thanks to my little girl Kelthoum who will always be my flesh and blood attachment to the United States of America.

TABLE OF CONTENT

DEDICATION iii
 ACKNOWLEDGMENTS iv
 LIST OF TABLES viii
 LIST OF FIGURES ix
 ABSTRACT xii

CHAPTER PAGE
 INTRODUCTION 1

CHAPTER 1: A STATISTICAL ASSESSMENT OF THE LOCAL WIND-DRIVEN
 RESPONSE 3
 1.1 Introduction 3
 1.2 Atmospheric forcing 6
 1.3 Statistical analysis 8
 1.3.1 Data selection 8
 1.3.2 Empirical mode analysis 12
 1.3.3 Spectral analysis 13

CHAPTER 2: A TWO-LAYER WIND-DRIVEN CHANNEL CIRCULATION
 MODEL 27
 2.1 Introduction 27
 2.2 Model governing equations 27
 2.2.1 Coastal jet 27

2.2.2	Channel jet	28
2.2.3	Analytical solution	32
2.2.4	Longshore steady wind forcing	40
2.3	Discussion	42
CHAPTER 3: FRICTIONAL ADJUSTMENT NUMERICAL MODEL		50
3.1	Governing equations	50
3.2	Analytical steady state solution	52
3.3	Numerical model	54
3.3.1	Choice of parameters	58
3.3.2	Model results and discussion	60
CHAPTER IV: CONCLUSION		72
REFERENCES		78
APPENDIXES		82

LIST OF TABLES

	PAGE
Table 1.1 Percent variance carried by EOF mode 1 and 2 at stations TN and TC.	13
Table 1.2 Partition of 100% of the current component U (and V) variance with respect to the two forcings at frequency 0.0057 cph.	22
Table 2.1 Typical data of Gibraltar Strait channel jet.	47

LIST OF FIGURES

		PAGE
1.1	Bathymetry of the Strait of Gibraltar (Bormans and Garret, 1989), showing the location of moored Doppler Acoustic Profiling Current Meters (DAPCMs).	4
1.2	The vertical structure of EOF current mode 1 and 2 at the Tarifa North station.	10
1.3	The vertical structure of EOF current mode 1 and 2 at the Tarifa Center station.	11
1.4	From top, TN time series of atmospheric pressure difference ΔPa (dbar), wind stress τ (Pa) and current EOF mode 1 U component (m/s).	15
1.5	From top, TN time series of atmospheric pressure difference ΔPa (dbar), wind stress τ (Pa) and current EOF mode 1 V component (m/s).	16
1.6	Subtidal autospectra of U and V current EOF mode 1 and 2 amplitude time series ASMODnx, of atmospheric pressure difference ASATMPGRAD and of wind stress ASTAUU at Tarifa North.	18
1.7	The coherence amplitude and phase plus transfer function between the U current (left) and the V current (right) EOF mode 1 components and wind stress τ_u .	19
1.8	The coherence amplitude and phase plus transfer function between the U current (left) and the V current (right) EOF mode 1 components and atmospheric pressure difference ΔPa .	20

1.9	Ordinary (OC), multiple (MC) and partial (PC) coherences between current EOF mode 1 U component (U), wind stress (W) and atmospheric pressure difference (P) at location Tarifa North. The partial coherence exclude one forcing (_W or _P).	23
1.10	Ordinary (OC), multiple (MC) and partial (PC) coherences between current EOF mode 1 V component (V), wind stress (W) and atmospheric pressure difference (P) at location Tarifa North. The partial coherence exclude one forcing (_W or _P).	24
1.11	100% variance distribution for current U mode 1.	25
1.12	100% variance distribution for current V mode 1.	26
2.1	Schematic picture of Channel jet development in two-layer fluid for a channel width equal to the internal Rossby radius R_2 . The characteristic elements of the flow are the densities ρ_i , the depths h_i , and the seasurface and interface ζ_i , where i is the layer index: $i=1$ for the upper layer and $i=2$ for the lower one.	29
2.2	Seasurface and interface elevations versus a normalized cross section position. The elevations are for a 15 km (straight line) and 150 km (dotted line) channel width.	48
2.3	Longshore average velocities versus the normalized cross section position. A 15 km (straight line) and 150 km (dotted line) channel width are presented.	49
3.1	Staggered space-time grid for numerical model. At filled square grid points, the 2 cross-shore average velocities v_1 and v_2 are unknown, and similarly at empty grid points u_1 , u_2 , ζ_1 and ζ_2 are to be determined.	56

3.2	Interface elevation space-time distribution computed for a channel width of $10 R_2$: (a) 3D view of the discretized matrix $\zeta_2(i,j)$ where i and j represent the index for space steps and time steps respectively; (b) closest to shores $i=1$ and $i=N_y-1$ time profiles of ζ_2 . In both plots, the profile in dashed line is interpolated along the channel axis ($y=0$).	61
3.3	Upper layer longshore averaged velocity distribution in space-time computed for a 150 km channel width: (a) 3D view of the discretized matrix $u_1(i,j)$ where i and j represent the index for space steps and time steps respectively; (b) closest to shores $i=1$ profile vs time. Since the velocity distribution is symmetric with respect to the channel axis, only this plot is shown. In both plots, the profile in dashed line is interpolated for the channel axis ($y=0$).	62
3.4	Space-time distributions of the channel flow upper layer components for a channel width of $10R_2$ (150 km).	65
3.5	Space-time distributions of the channel flow lower layer components for a channel width of $10R_2$ (150 km).	66
3.6	Space-time distributions of the channel flow upper layer components for a channel width of R_2 (15 km).	67
3.7	Space-time distributions of the channel flow lower layer components for a channel width of R_2 (15 km).	68
3.9	Two-layer schematic cross-section for the adjustment over bathymetry.	70

ABSTRACT

WIND-DRIVEN OBSERVATION AND MODELLING IN THE STRAIT OF GIBRALTAR

by

Abdelkader Benabdeljelil
University of New Hampshire, December, 1994.

Meteorological forcing has been found to be responsible for 65% of the subtidal current variance through Gibraltar Strait. However this value does not discriminate between atmospheric pressure and wind. Conditional coherences applied to a 2-input/single output system are computed to distribute the total variance of current data from the Gibraltar Experiment into wind-only, pressure-only, noise and shared forcings. Evidence is presented which shows that, within the subtidal range, wind and atmospheric pressure force the flow equally.

This study focuses on understanding the dynamics of the wind-driven circulation in a 2-layer channel. A channel jet model proves to be very useful in explaining the dynamic balance in each of the two layers, but for relatively short time scales. To overcome this weakness, friction stresses are included, for which a steady state solution appears as an intriguing slab-flow. Numerical analysis is used to understand the dynamic processes which take place between

the short time scale channel jet solution and the long-term steady state solution. The flow structure through Gibraltar Strait is shown to reach steady state in approximately one day.

Introduction

Channel wind-driven flow occurs in a variety of practical and geophysical situations. Gibraltar Strait offers the possibility to investigate the dynamics of such flow.

Oceanographic and meteorologic data collected during the Gibraltar Experiment (1985 to 1987) have brought the exchanges through the strait under new light. A combination of factors driving the flow have been assessed. Among them the wind drag is still under investigation. However, little attention have been focused on the dynamics following the onset of wind forcing of a two-layer channel.

At first, a statistical approach is proposed to assess the wind influence on the flow. The current variance, in the subtidal frequency range, is distributed among two meteorological forcings, wind and atmospheric pressure.

In order to understand the dynamics behind a wind-driven two-layer channel flow, a first simplified set of momentum equations is solved analytically in Chapter 2. Although the hypotheses considered in this part are highly restrictive, the model results reveal the main features of the channel wind-driven circulation for short time scales. The major deficiency of such model arises from the absence

of interfacial and bottom friction in its momentum equations. A second model incorporating these stresses is then studied in Chapter 3. A numerical analysis helps elucidate the flow evolution from the channel jet solution to the steady state solution.

CHAPTER 1

A Statistical Assessment of the Local Wind-Driven Response

Oceanographic and meteorologic data collected during the Gibraltar Experiment (1985 to 1987) have brought the exchanges through the strait under new light. A combination of factors driving the flow have been assessed, among them the wind drag is still under investigation. A first statistical approach to the estimation of the wind influence on the flow is proposed.

1.1 Introduction

The Strait of Gibraltar separates Europe from Africa and is the only avenue of exchange between the Alboran Basin on the Mediterranean side and the Gulf of Cadiz on the Atlantic side. Under the surface, a sill, located between Punta Paloma (Spain) and Punta Altares (Morocco) is the most prominent feature of the western bathymetry of the Strait. It acts as a ridge or an underwater dam and extends over the whole cross-section with a relatively shallow maximum depth of approximately 300 m. Above the sea level, the coastal topography presents a channel-like configuration for atmospheric forcing such as the highly seasonal easterly Levantine winds which predominate in the area and are polarized in the along strait direction. These winds are

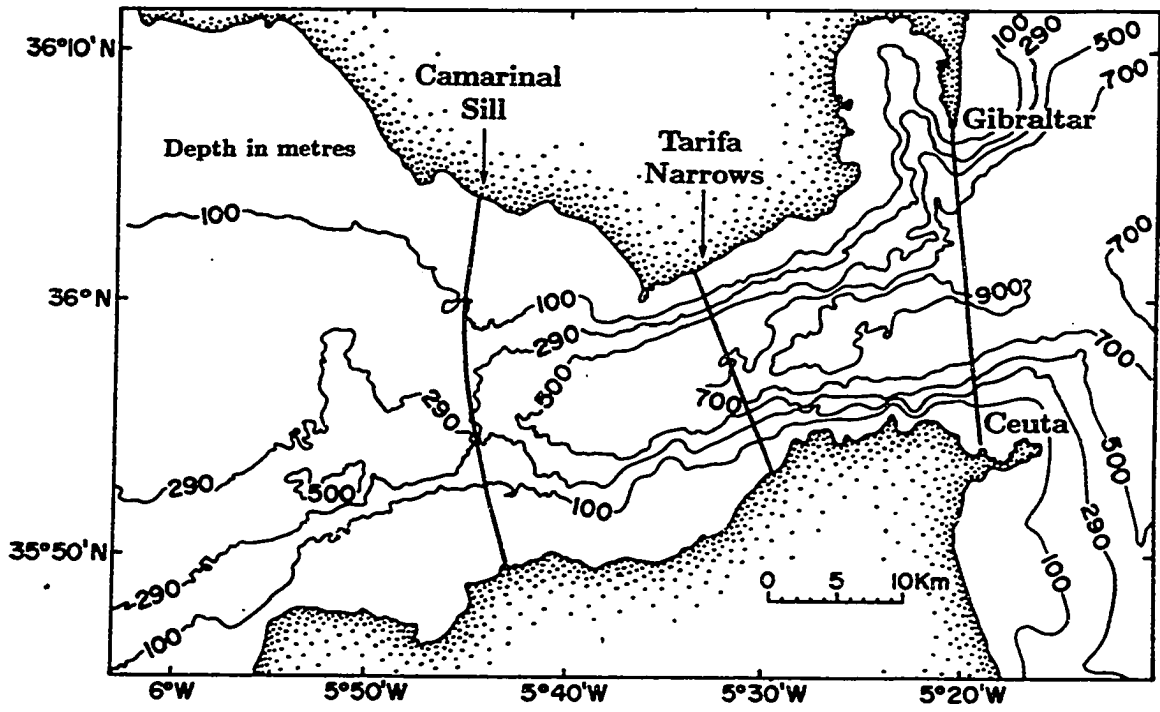


Figure 1.1: Bathymetry of the Strait of Gibraltar (Bormans and Garret, 1989), showing the location of moored Doppler Acoustic Profiling Current Meters (DAPCMs).

notably strong and sometimes exceed 25 ms^{-1} for a few days (Dorman 1988).

In a landmark publication, Lacombe and Richez (1982) have suggested that the most important flow fluctuations through the Strait of Gibraltar may be subdivided into: tidal, subtidal, and long-term. This classification scheme has been used by Candela (1989) who showed that fluctuations in each of these regimes have similar magnitudes (from 0.5 to 1.0 ms^{-1}). The long-term flow exhibits seasonal and interannual variability, and relates to the two-layer baroclinic (depth dependent) exchange. It reflects mainly the density driven net fluxes through the Strait produced by the excess evaporation (relative to precipitation and runoff) over the Mediterranean Sea (Bethoux 1979 and 1980). For these long time scales, some of the models used to estimate the relatively large magnitudes of the inflow and outflow suggest transports around 1 to 2 Sv ($1 \text{ Sv} = 10^6 \text{ m}^3 \text{ s}^{-1}$), as described by Bryden and Kinder (1988).

The characteristics of the main regime are relatively well known. To this regime, complex phenomena are superimposed resulting from tides (including an internal tidal bore), atmospheric pressure field over the Mediterranean Sea, local winds, internal mixing between layers and seasonal variation in the barotropic and baroclinic along strait pressure gradients.

Although conceptually simple, the foregoing

classification of the flow through the Strait does not account for appreciable nonlinear interactions that can occur between the different flow regimes. In particular the high correlation found between depth fluctuations of the interface separating the Atlantic and Mediterranean waters, and barotropic flows at the sill, both at tidal and subtidal frequencies, imply appreciable net transports (Bryden et al. 1988; Candela et al. 1989). This relation has also been tested by Pettigrew and Hyde (1989) who estimated that the steady component of the Strait circulation actually carries only 40% of the mean Atlantic inflow in the Tarifa Narrows, the remaining 60% being attributed to a combination of nonlinear and nonsteady flows.

Subtidal flows, with periods ranging from days to a few months, are principally forced by atmospheric factors such as the atmospheric pressure systems propagating over the entire Mediterranean (Crépon 1965; Garrett 1983) and the local winds (Lacombe and Richez 1982). Candela's analysis revealed a root mean square transport of nearly 0.4 Sv for the combined wind-pressure forced regime in a mostly barotropic flow (Candela et al. 1989).

1.2 Atmospheric Forcing

Much of the research about atmospheric forcing has dealt solely with the atmospheric pressure field over the Mediterranean basins (Crépon 1965; Candela 1989; Garrett

1983; Garrett et al. 1984). The literature, however, exhibits conflicting evidence as to the role of wind-stress in driving the flow through the Strait of Gibraltar regime. Several studies (Bryden and Stommel 1984; Bormans et al. 1986) speculate on the possible forcing of the seasonal fluctuations by the wind and the wind's influence on the long-term highly baroclinic flow. Candela (1989) estimated that 65% of the total current variance at subinertial frequencies was related to forcing by the atmospheric pressure field over the Mediterranean Sea. However his computations do not take into account the correlation between the wind and the atmospheric pressure gradient, and hence include in this estimate an unknown portion that may be directly driven by the wind.

Both tidal and subtidal variations are mainly barotropic, although a strong baroclinic contribution has been identified in the Tarifa narrows (Pettigrew and Hyde, 1989). Candela (1989) estimated that 84% of the variance observed at subtidal frequencies to be depth-independent. However, there is some question whether the data analyzed included observations to adequately characterize the upper layer. He also believed that part of the depth dependence that was observed is due to the local winds over the Strait. From their observations, Lacombe and Richez (1982) suggested that the wind influence is confined mainly to the upper 20 m, where it may induce currents as large as 0.5 ms^{-1} in the

direction of the wind, strong enough at times to reverse the current flow upwind.

The true role of the wind in driving the flow remains a subject of debate, and virtually no thought has been given to its dependence on both along and across-strait positions. It is well understood that a wind blowing along a coastline has strong effect on the current field of the location (Csanady, 1977, 1982). Therefore winds, as strong as those encountered in the Strait of Gibraltar (Dorman 1988), might be expected to have marked influence on the regime of the Strait.

1.3 Statistical Analysis

1.3.1 Data selection

Gibraltar Experiment current data have been collected using two types of instruments: conventional moored current-meters (MCM) and remote-sensing Doppler Acoustic Profiling Current-Meters (DAPCM). The drag on the MCMs in the energetic Gibraltar Strait induced large vertical displacement (60 m) of the instruments. Statistical analysis of the records revealed no significant relationship between wind and currents; a situation ascribed to low signal to noise ratio. On the other hand, the DAPCM, well anchored on the bottom in the narrowest section of the channel, provided current measurements at fixed depths. The hourly averaged records are obtained along a water column profile every 8 m

from the depth of 120 m in a location named Tarifa-North (TN in Figure 1.1) and every 10 m over a depth of 240 m in Tarifa-Center (TC in Figure 1.1).

The wind data considered in this study were obtained from the Spanish authorities and consist of wind velocity component values measured every 6 hours at Castilla-Tarifa, a station about 6 km west of Tarifa-North where the DAPCM was deployed. The raw wind data have been interpolated to hourly values using a cubic spline. The wind stress components are computed using a quadratic drag formula (Gill, 1982; Wu, 1980 and 1982):

$$\tau = C_D \rho_{\text{air}} \|u_w\| u_w$$

where:

u_w is the wind velocity,

C_D the drag coefficient defined as:

$$10^3 C_D = 1.1 \text{ for low wind speed and}$$

$$10^3 C_D = 0.61 + 0.063 \|u_w\| \text{ for } 6 \text{ ms}^{-1} < \|u_w\| < 22 \text{ ms}^{-1},$$

ρ_{air} the air density has a value of 1.2 kg/m^3 .

The Castilla wind fluctuations are effectively polarized in the east-west direction; its principal component is oriented along the Strait axis. Hence, one need only consider the alongstrait wind stress component τ_x as representative of the wind stress variability in the Strait.

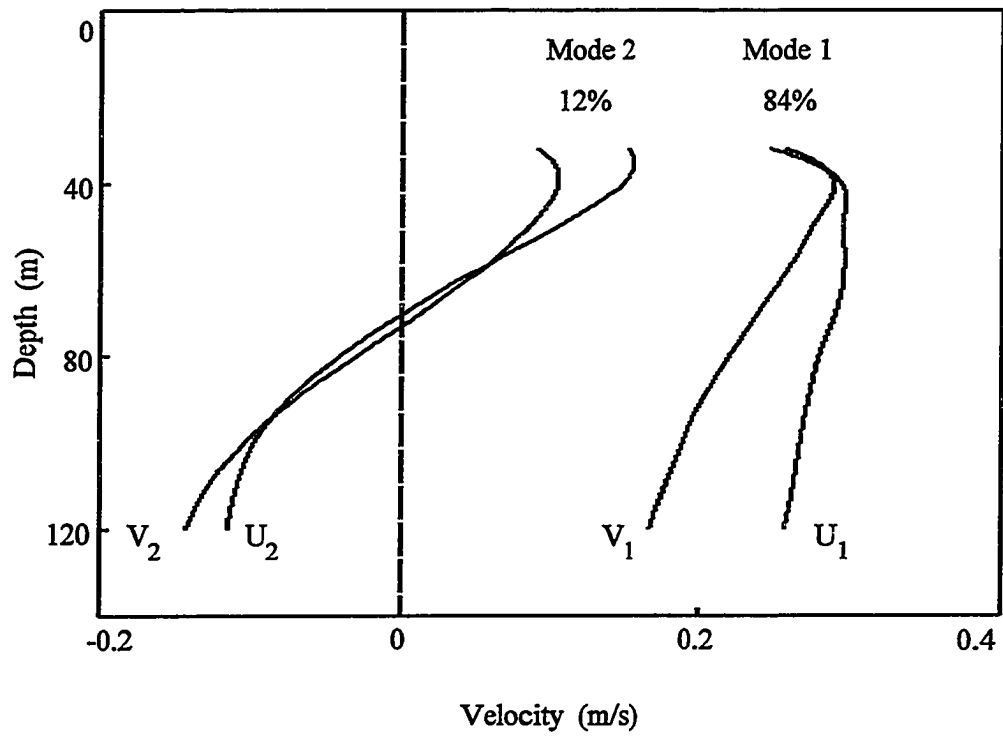


Figure 1.2: The vertical structure of EOF current Mode 1 and 2 at the Tarifa North station.

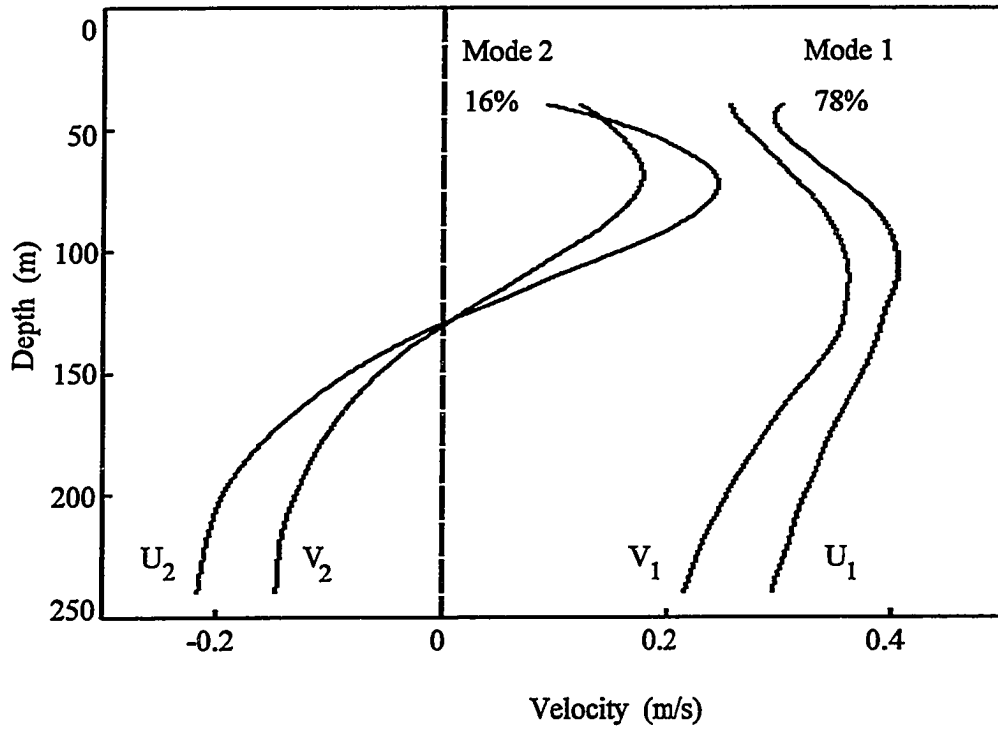


Figure 1.3: The vertical structure of EOF current Mode 1 and 2 at the Tarifa Center station.

Atmospheric pressure data from two locations have been selected from data obtained from the European Center for Medium Range Forecasting; data from Almeria Spain (at the northeastern entrance to the Alboran Basin) and at Sagres Portugal (in the northeast of the Gulf of Cadiz). Like for the wind record, the 6-hourly meridional difference has been interpolated to hourly data.

1.3.2 Empirical Mode Analysis

In order to streamline the time series analysis of the covariance of currents (at many depths) and atmospheric forcings, a variation of the method of Empirical Orthogonal Function (EOF) analysis (Kundu et al. 1975) was used. This method is useful for finding statistically independent modes of motion for the entire current profile and generating the appropriate modal time series, rather than analyzing the current depth by depth. For the analysis presented here, an extension of the standard method has been developed (Appendix 1.1). This modified method allows a unified treatment of vector time series as complex time series when applied to current vector time series over a range of depths. The EOF analysis method extracts the correlated patterns of the variance behavior of the currents vectors over the entire water column based on their statistics.

As shown in Table 1.1, two modes contribute 96% of the total variance in TN and 94% in TC. Although the vertical

weight distributions associated with these two modes reflect only on the variances of the current components U and V, it shows quasi-uniform mode 1 profiles and strong shear mode 2 profiles for both stations (Figure 1.2 and 1.3). Each of these weights describes the percentage of the total variance carried by the corresponding time series, hence the sign of the weight distribution related to the second mode characterizes only the baroclinic structure of the currents along the water column while the first mode weight distribution illustrates the strong barotropic current profile.

	TN	TC
EOF Mode 1	84%	78%
EOF Mode 2	12%	16%

Table 1.1: Percent variance carried by EOF mode 1 and 2 at stations TN and TC.

1.3.3 Spectral Analysis

The ordinary, multiple and partial coherence terms, phase and gain between forcings and current modes are computed using a spectral averaging routine of 50% overlapping pieces (Nuttall 1971) to increase the number of degrees of freedom. Accordingly the 95% confidence limit of the coherences is derived from the number of equivalent degrees of freedom (Gilbert, 1990):

$$\text{EDF} - 3.82 \frac{T}{M} - 2.24$$

where T is the length of the time series and M is the block length.

The TC current times series extend only over five weeks. Consequently they do not produce any statistically significant coherences relative to the large statistical uncertainties. Hence these results are not discussed further here and all following discussion focuses only on the longer current time series from station TN.

The time series of the variables considered are presented in Figures 1.4 and 1.5. The mean of each of the overlapped pieces has been removed to help ameliorate the effects of nonstationarity of the times series. Although the high frequency variations of the current mode 1 EOF amplitude time series (bottom plot) tend to hide its subtidal variability, the plot clearly suggests some level of correlation between the wind stress τ , the atmospheric pressure difference ΔPa , and the current.

The autospectra of the U and V current component EOF mode 1 and 2 amplitude time series and those of the wind and atmospheric pressure difference are presented for the subtidal frequency range in Figure 1.6. The overall slope of the three spectra are similar.

The ordinary coherences between time series of current

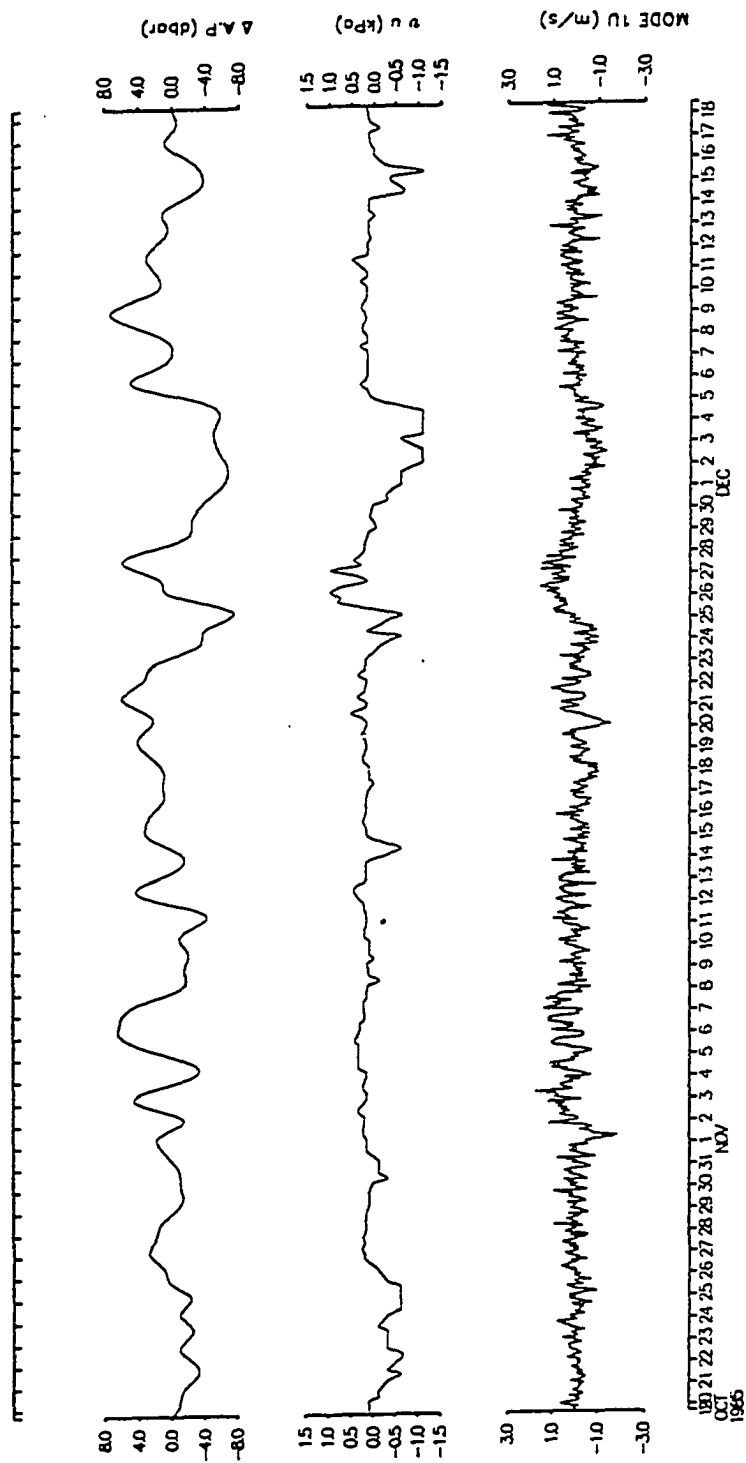


Figure 1.4: From top, TN time series of atmospheric pressure difference ΔP (dbar), wind stress τ (Pa) and amplitude time series current EOF mode 1 U component (m/s).

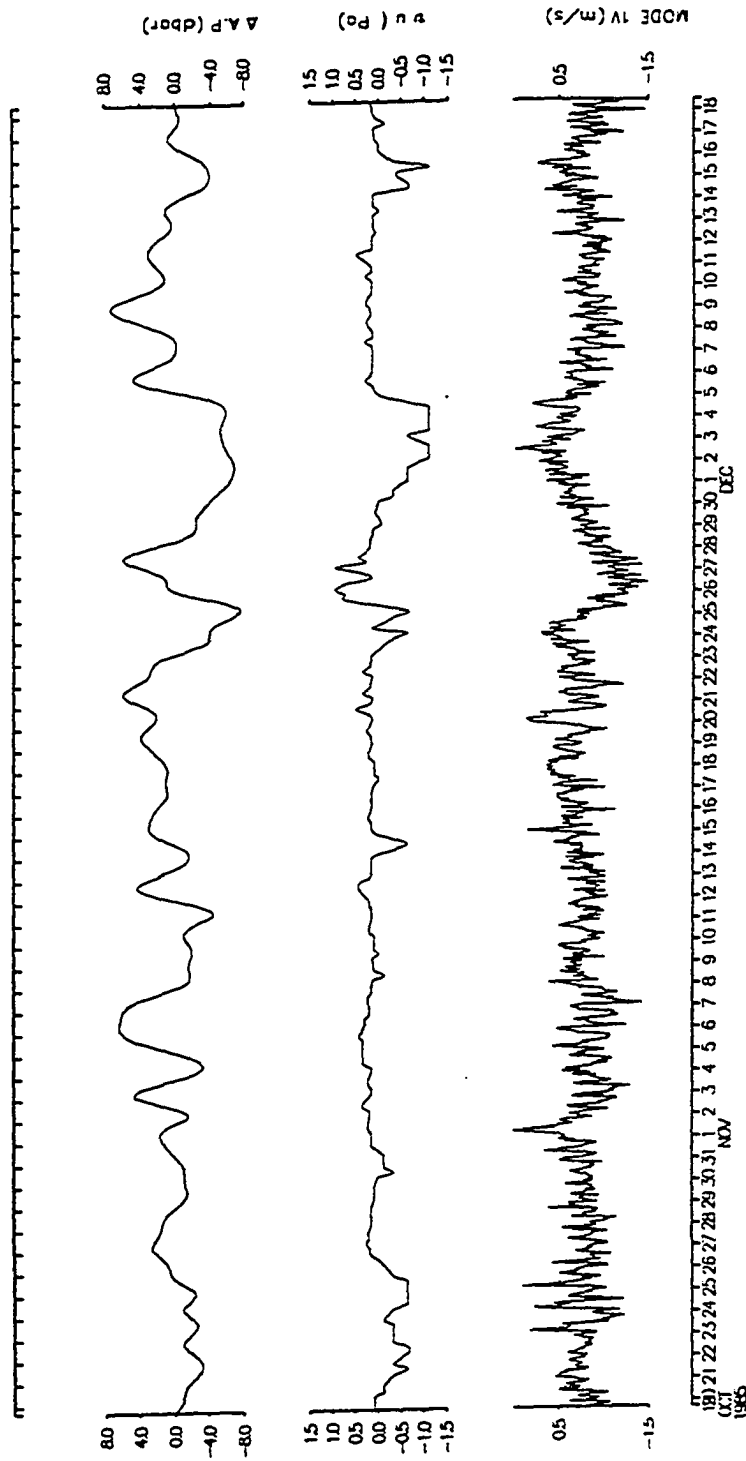


Figure 1.5: From top, TN time series of atmospheric pressure difference ΔP (dbar), wind stress τ (Pa) and amplitude time series current EOF mode 1 V component (m/s).

EOF mode 1 and 2 components U and V, atmospheric pressure difference and wind stress are computed for subtidal frequencies (period between 50 and 400 hours). Significant coherences (Figure 1.7 and 1.8) between any two of these variables are found above the 95% confidence level. The phase and gain error estimates are calculated according to Bendat and Piersol (1986).

There is no coherence between mode 1 or 2 (U and V components) and the wind stress, nor between the wind stress and the atmospheric pressure difference for subtidal frequencies between 0.02 cph and 0.012 cph. The phase, for frequencies below 0.02 cph, presents an interesting feature. If the forcings are in phase with each other, the mode 2 velocity components are both out of phase (by 180°) with the wind stress and the atmospheric pressure gradient in the frequency bands where there is significant coherence.

These considerations ignore the fact that coherences between the wind stress and the atmospheric pressure difference may exist. To address this issue, partial and multiple coherences are computed (Figure 1.9 and 1.10) (Appendix 2) in order to discriminate between that part of the current variance forced only by the wind, that part forced only by the atmospheric pressure, and the part which is forced by both (wind-atmospheric pressure shared forcing). By translating the different coherence values as percentages of the current variance, one can compute the

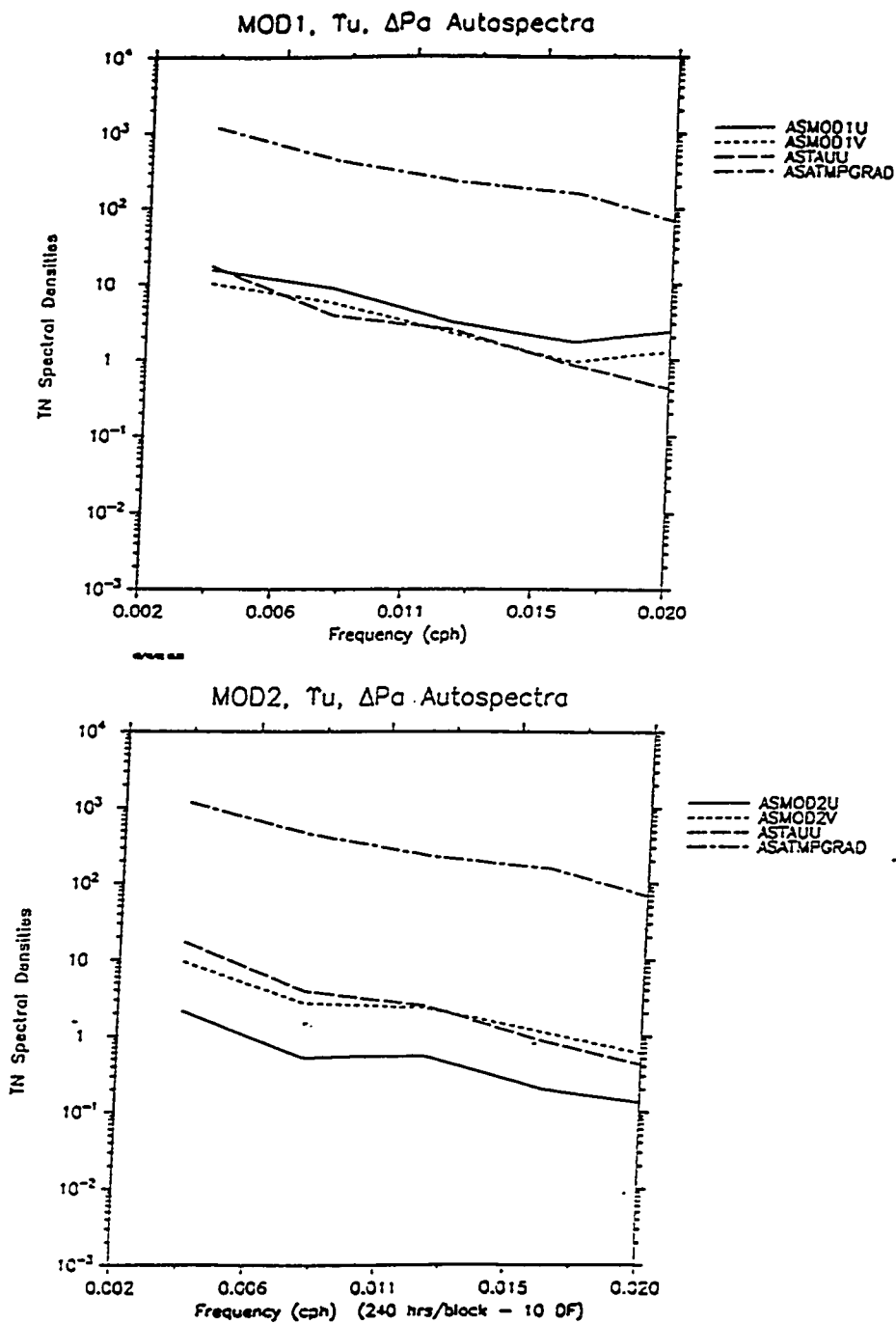


Figure 1.6: Subtidal autospectra of U and V current EOF mode 1 and 2 amplitude time series ASMODnx, of atmospheric pressure difference ASATMPGRAD and of wind stress ASTAUU at Tarifa North.

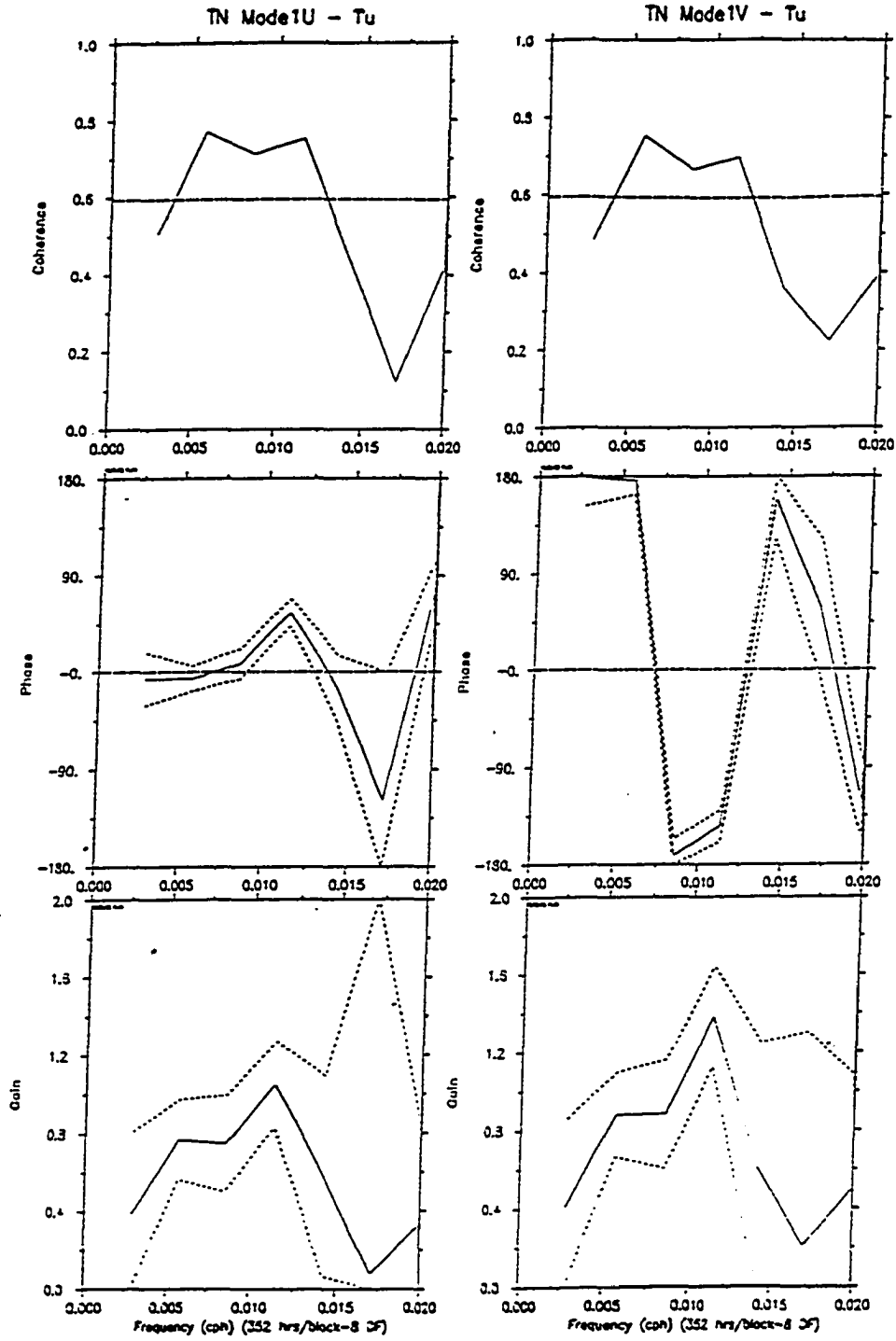


Figure 1.7: The coherence amplitude and phase plus transfer function between the U current (left) and the V current (right) EOF mode 1 components and wind stress τ_u .

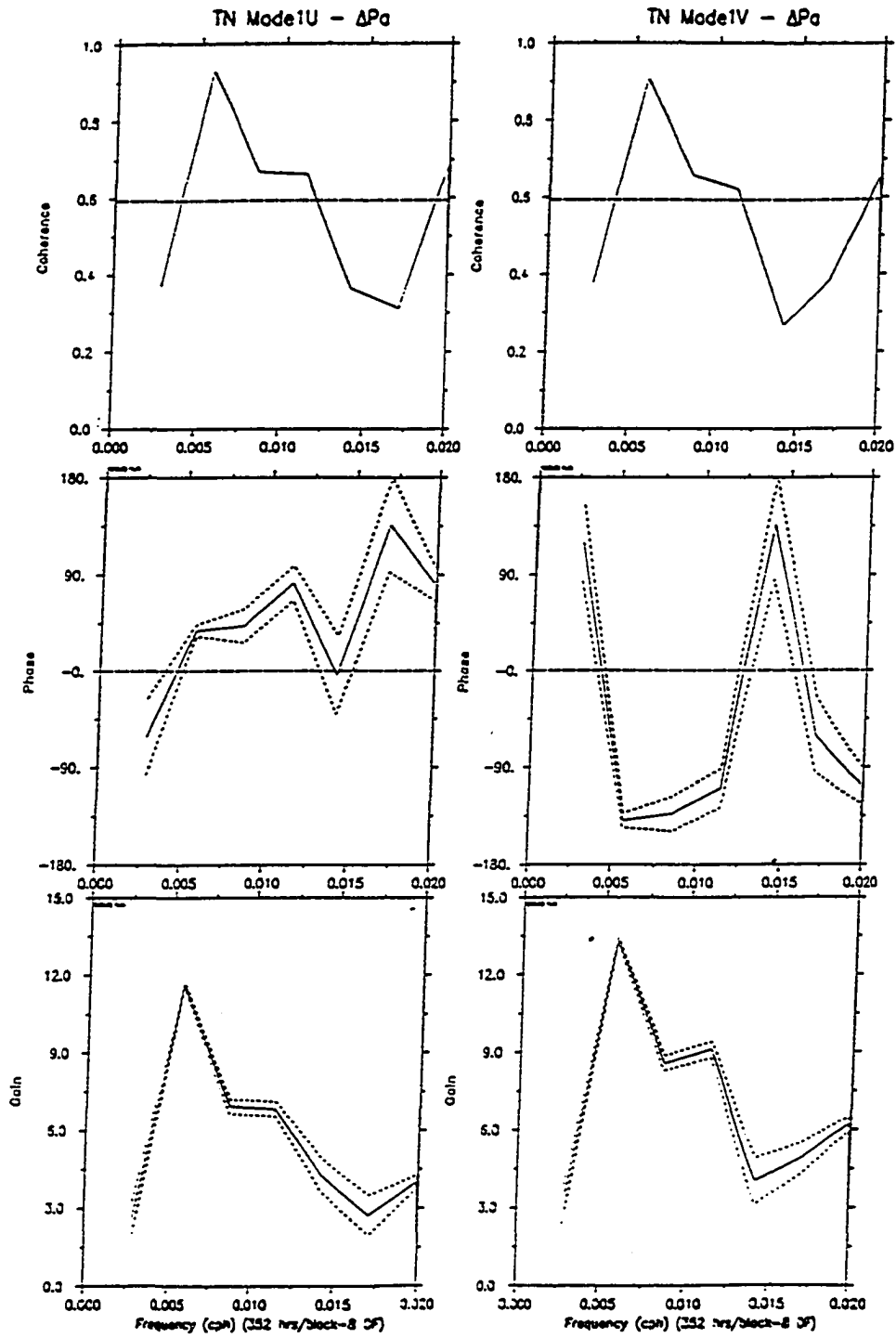


Figure 1.8: The coherence amplitude and phase plus transfer function between the U current (left) and the V current (right) EOF mode 1 components and atmospheric pressure difference ΔPa .

amount of forcing due to the wind-only, the atmospheric pressure-only and the shared forcing.

The decomposition of the current EOF mode 1 components variance due to different forcing are displayed in Figure 1.11 and 1.12 respectively. Whenever the ordinary coherence values are found above the 95% significance test and for frequencies between the lowest resolvable band and the upper subinertial band, the total variance is displayed as 100% (the y-coordinate of Figures 1.11 and 1.12) and distributed between the wind-only, the pressure-only and the shared forcing (Table 1.2). Above the shared wind-pressure percentage level resides the portion of the variance attributed to the noise, which includes all forcings other than the wind and the atmospheric pressure.

These statistical results establish for the first time that the wind, taken as a distinct forcing from the atmospheric pressure, is responsible for driving a significant part of the current variability at this subtidal frequency. Thus it is as quantitatively important as the atmospheric pressure and regardless of how much variance wind and atmospheric pressure drive undissociably. In fact, considering the wind-only and the shared forcing, the wind forcing may account for approximately 60% of the variance in the subtidal frequency band.

Wind-only 19% (24%)	Noise 16% (15%)
Shared forcing Wind & Pressure 48% (38%)	Atmospheric pressure-only 17% (23%)

Table 1.2: Partition of 100% of the current component U (and V) variance with respect to the two forcings at frequency 0.0057 cph.

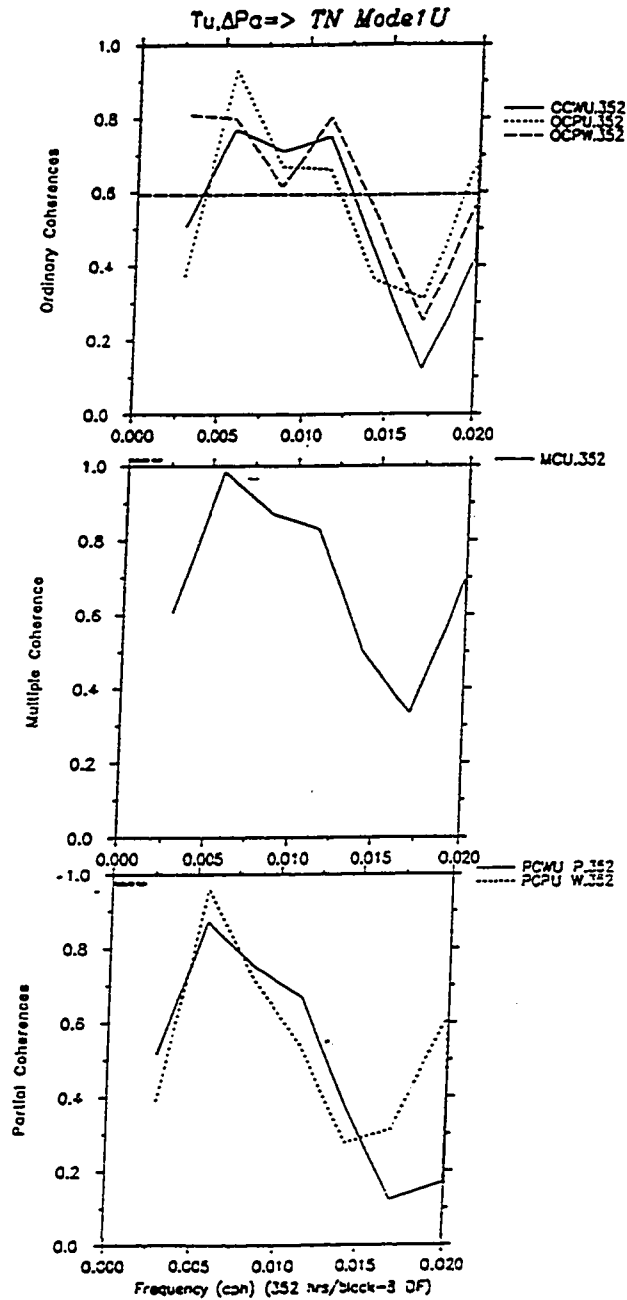


Figure 1.9: Ordinary (OC), multiple (MC) and partial (PC) coherences between current EOF mode 1 U component (U), wind stress (W) and atmospheric pressure difference (P) at location Tarifa North. The partial coherence exclude one forcing ($_P$ or $_W$).

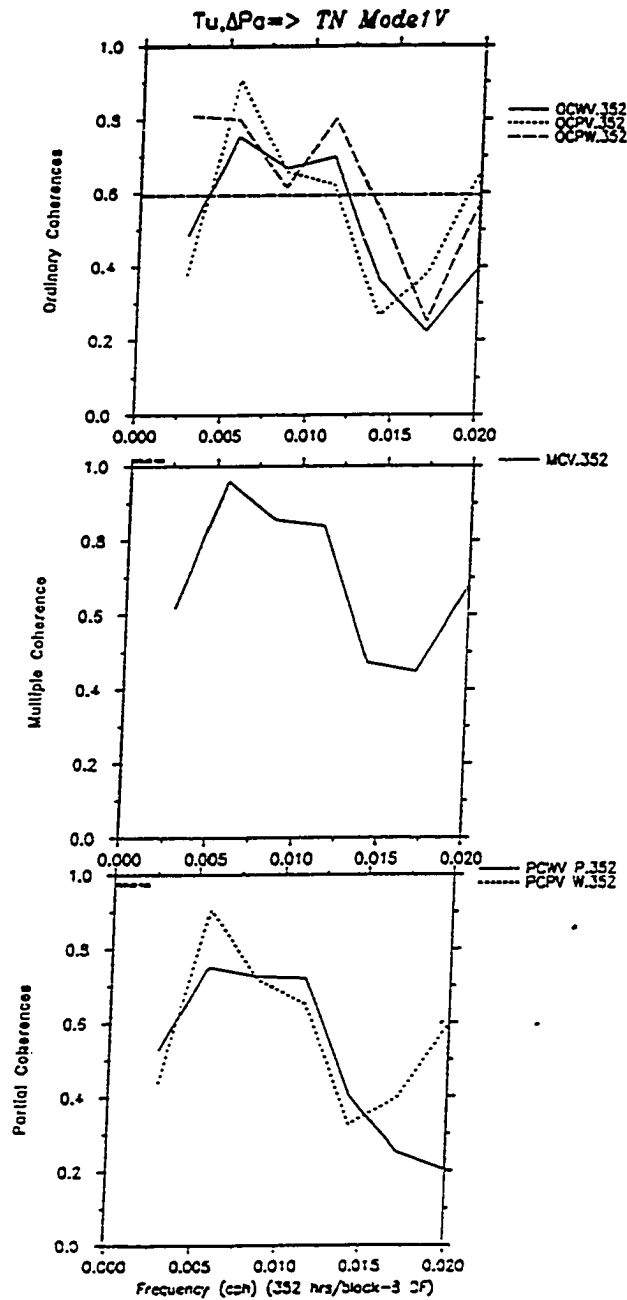


Figure 1.10: Ordinary (OC), multiple (MC) and partial (PC) coherences between current EOF mode 1 V component (V), wind stress (W) and atmospheric pressure difference (P) at location Tarifa North. The partial coherence exclude one forcing (_P or _W).

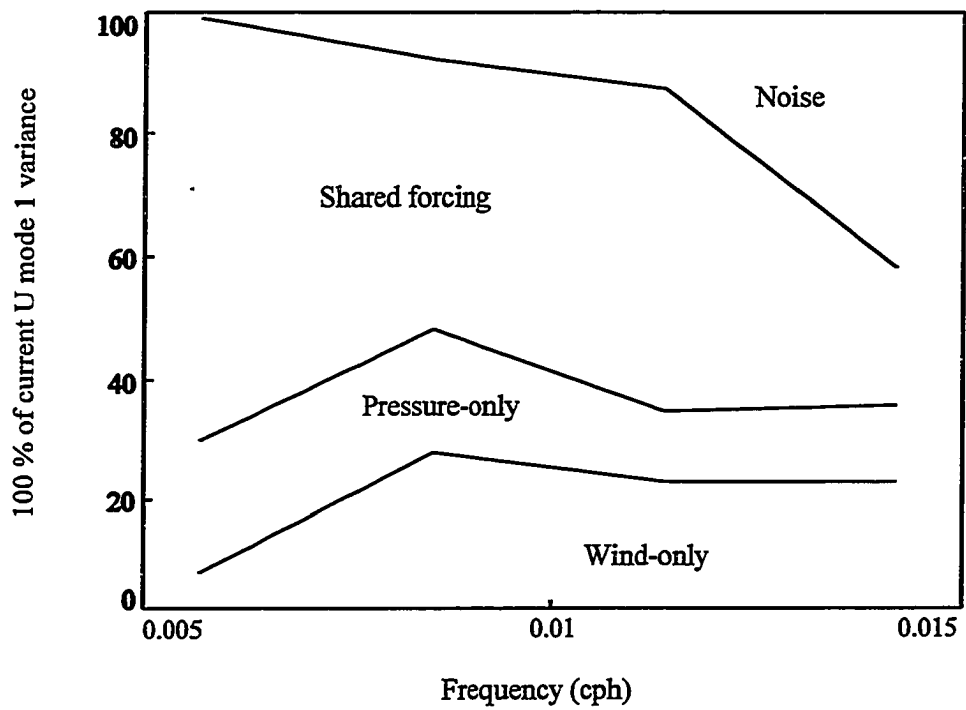


Figure 1.11: 100% variance distribution for current U EOF mode 1

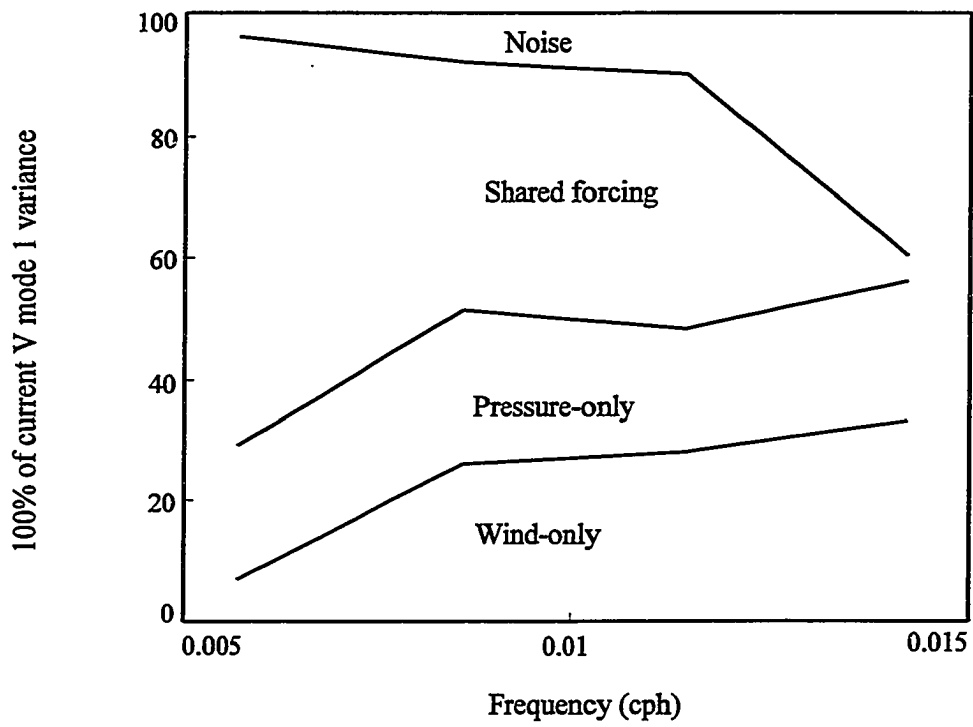


Figure 1.11: 100% variance distribution for current V EOF mode 1

CHAPTER 2

A Two-Layer Wind-Driven Channel Circulation Model.

2.1. Introduction

In the Strait of Gibraltar the fluid motions are of great complexity depending on a large number of internal and external parameters. Moreover, the diversity of forcings as well as the configuration of the channel bathymetry suggest complicated motions such that their statistics may not adequately represent or illuminate the strait dynamics.

A theoretical tool to challenge this situation is the 'conceptual model' (Csanady, 1977, 1982). The case of wind-driven flow in the Strait of Gibraltar is a phenomenon that can benefit from the application of a conceptual model since little attention has been given to the problem of wind driven currents in the Strait, and debate persists about its physical and dynamical characteristics. The analytical model proposed in this chapter focuses only on reproducing predominant features of the flow dynamics and is purposely incomplete.

2.2. Model governing equations

2.2.1. Coastal Jet

Charney (1955) was the first to propose the Coastal Jet denomination in a discussion of geostrophic adjustment near

a coast line for the Gulf Stream. Describing a two-layer flow dynamics under a wind forcing, the model was later successfully applied to local wind-driven coastal currents (Crepon 1969 and 1971), in the Great Lakes (Csanady, 1972 and 1973) and in coastal boundary regions (Pettigrew, 1981; Pettigrew and Murray, 1986).

2.2.2. Channel model

In this study we couple two facing coastal jets on either side of the channel for a stratified two-layer fluid flow. The physical problem being considered is illustrated schematically in Figure 2.1. A right-handed Cartesian coordinate system is chosen with x being along-channel, y being across channel horizontal axes and z the vertical axis with $z=0$ at the still water level. The channel has a flat bottom and vertical walls. The surface and interface deformations are ζ_1 and ζ_2 respectively, while ρ_i and h_i are the density and water depth appropriate to the i -th layer.

In the derivation of the governing equations, each layer is assumed to be well-mixed so that the water is homogeneous. Hence, the interface between the upper and lower water layers is hypothetical and is introduced because of a density difference. The model treats the flow in an intermediate depth channel of two depth-averaged layers. The vertical length scale H (h_1+h_2) as well as the channel width ($2a$) are much smaller than the length scale of the channel.

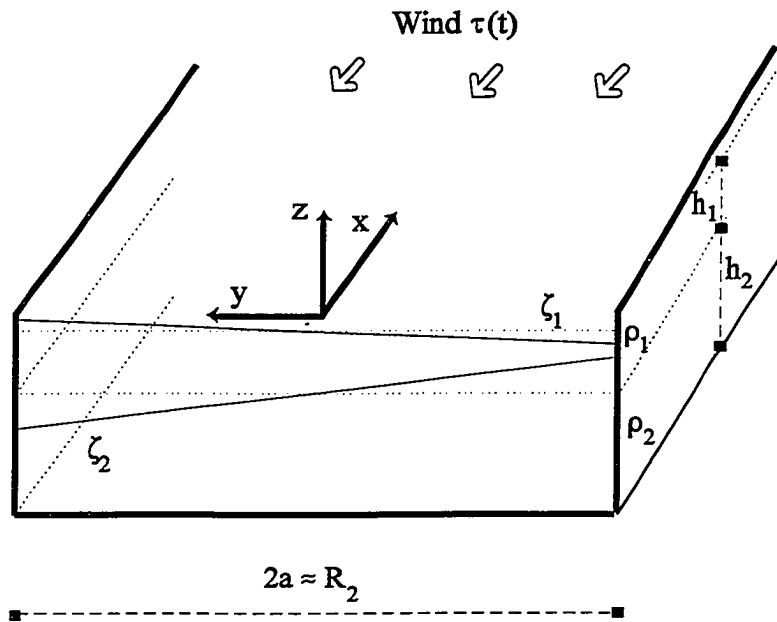


Figure 2.1: Schematic picture of Channel Jets development in two layer fluid for a channel width $2a$ equal to the internal Rossby radius R_2 . The characteristic elements of the flow are the densities ρ_i , the depths h_i , and the seasurface and interface ζ_i , where i is the layer index: $i=1$ for the upper layer and $i=2$ for the lower one.

From continuity, the vertical motion is negligible compared with the horizontal motions, and thus the vertical momentum equation simply reduces to the hydrostatic pressure distribution which, using the differential operator notation as an index, can be expressed as:

$$p_{i,z} = -\rho_i g$$

where p is the fluid pressure, ρ_i the water density of the i -th layer. The general Navier-Stokes equations, which in their nonlinear form are notoriously not solvable, are simplified for this case by neglecting the momentum advection terms because the ratio of the nonlinear terms to the Coriolis force (the Rossby number) is small compared to 1. Two-dimensional barotropic numerical models (Bennett and al., 1979) show that the neglect of nonlinear advective terms is probably not a serious limitation.

Integration of the continuity equation and horizontal momentum equations over the depth of each layer, then averaging over the appropriate depth together with applying the kinematic boundary conditions at the surface and the bottom ($w=0$ at $z=0$ and at $z=-H$), yields the layer averaged equations:

$$\left\{ \begin{array}{l} \bar{u}_{1,t} + 2\bar{\Omega} \times \bar{u}_1 - g \bar{\nabla} \zeta_1 + \frac{\tau_1}{\rho_1 h_1} \\ \nabla \cdot \bar{u}_1 = \frac{1}{h_1} (\zeta_{2,t} - \zeta_{1,t}) \\ \bar{u}_{2,t} + 2\bar{\Omega} \times \bar{u}_2 - g \bar{\nabla} [(1-\varepsilon) \zeta_1 + \varepsilon \zeta_2] + \frac{\tau_2}{\rho_2 h_2} \\ \nabla \cdot \bar{u}_2 = -\frac{1}{h_2} \zeta_{2,t} \end{array} \right. \quad (2.2)$$

where $2\bar{\Omega}$ is the earth's angular velocity, ε the proportional density defect defined by:

$$\varepsilon = \frac{\rho_2 - \rho_1}{\rho_2} \quad (2.3)$$

and τ_i the net stress terms applied respectively to each layer.

Assuming that a discrete pycnocline exists, the pressure terms are expressed in terms of surface and thermocline elevations above equilibrium, ζ_1 and ζ_2 , both assumed to be negligible compared to equilibrium layer thicknesses h_1 and h_2 :

$$\left\{ \begin{array}{l} p_1 = p_{\text{atm}} + \rho_1 g (\zeta_1 - z) \\ p_2 = p_{\text{atm}} + \rho_1 g (\zeta_1 + h_1 - \zeta_2) + \rho_2 g (\zeta_2 - z - h_1) \end{array} \right.$$

where p_{atm} is the atmospheric pressure. The along-shore wind stress is the only forcing considered in this case. The stress terms are then:

$$\begin{cases} \tau_1(t, y) = \tau_0(t) \bar{i} \\ \tau_2(t, y) = \bar{0} \end{cases}$$

where $\tau_0(t)$ is a wind stress applied at the surface. The channel depth H is assumed to be constant and the upper layer slightly lighter than the lower layer such that ϵ is of the order of 10^{-3} . The boundary conditions are that normal velocities are equal to zero at the coasts. A state of rest exists prior to the onset of wind forcing. Equations (2.2) compose the complete set for the two-layer circulation model: two continuity equations and four momentum equations to solve for six unknown quantities, namely the two layer averaged velocity vectors and two ζ_i .

2.2.3. Analytical solution

It is assumed that the model channel is of infinite length so that the partial x -derivative vanishes everywhere ($\partial/\partial x=0$).

The resulting system of equations is then:

$$\left\{ \begin{array}{l} u_{1,t} - f v_1 = \frac{\tau}{\rho_1 h_1} \\ v_{1,t} + f u_1 = -g \zeta_{1,y} \\ v_{1,y} = \frac{1}{h_1} (\zeta_{2,t} - \zeta_{1,t}) \end{array} \right. \quad (2.4)$$

$$\left\{ \begin{array}{l} u_{2,t} - f v_2 = 0 \\ v_{2,t} + f u_2 = -g [\varepsilon \zeta_{2,y} + (1-\varepsilon) \zeta_{1,y}] \\ v_{2,y} = -\frac{1}{h_2} \zeta_{2,y} \end{array} \right. \quad (2.5)$$

The momentum and continuity equations are coupled through the terms involving sea level ζ_1 and interface elevation ζ_2 . An easy way to reduce the number of derivations with respect to t or y is the Laplace transform. However, since the initial conditions are specified for $t=0$ while no condition exists at $y=0$ (center of the channel), the choice of t to be transformed is imposed.

Thus, the Laplace Transform versions of these equations with respect to t appear as:

$$\left\{ \begin{array}{l} p U_1 - f V_1 = \frac{\tau}{\rho_1 h_1} \\ p V_1 + f U_1 = -g Z_{1,y} \\ V_{1,y} = \frac{p}{h_1} (Z_2 - Z_1) \end{array} \right. \quad (2.6)$$

$$\begin{cases} pU_2 - fV_2 = 0 \\ pV_2 + fU_2 = -g[\varepsilon Z_{2,y} + (1-\varepsilon)Z_{1,y}] \\ V_{2,y} = -\frac{p}{h_2}Z_2 \end{cases} \quad (2.7)$$

In each set, U and V can be eliminated in favor of Z, thus resulting in:

$$\begin{cases} Z_2 - Z_1 + \frac{g h_1}{p^2 + f^2} Z_{1,yy} = 0 \\ Z_2 - \frac{g h_2}{p^2 + f^2} [\varepsilon Z_{2,yy} + (1-\varepsilon)Z_{1,yy}] = 0 \end{cases} \quad (2.8)$$

Eliminating Z_2 , the system leads to a single fourth order equation in Z_1 :

$$Z_1 - g \frac{h_1 + h_2}{p^2 + f^2} Z_{1,yy} + \varepsilon g^2 \frac{h_1 h_2}{(p^2 + f^2)^2} Z_{1,yyyy} = 0 \quad (2.9)$$

This equation can be solved directly, instead of generating a potential function for Z_1 (as done by Crepon, 1965, Csanady, 1977 and 1982, Pettigrew, 1981). Assuming the general solution in the form:

$$Z = e^{\delta m y}$$

where $\delta = \pm 1$, to characterize the facing coastal jets on either side of the channel. Equation (2.9) associated characteristic polynomial appears as a second order algebraic equation in m , the discriminant of which is Stoke's equation:

$$1 - g \frac{h_1 + h_2}{p^2 + f^2} m^2 + g^2 \varepsilon \frac{h_1 h_2}{(p^2 + f^2)^2} m^4 = 0$$

To the first order in ε , the eigenvalues of the above appear as:

$$\left\{ \begin{array}{l} m_1^2 = \frac{1}{h_1 + h_2} \frac{p^2 + f^2}{g} \\ m_2^2 = \frac{h_1 + h_2}{h_1 h_2} \frac{(p^2 + f^2)}{g \varepsilon} \end{array} \right.$$

Hence the two solutions for Z_1 are:

$${}^i Z_1 = e^{\delta \sqrt{p^2 + f^2} \frac{y}{c_i}} \quad i=1, 2 \quad (2.10)$$

where

$$\begin{cases} c_1 = \sqrt{g (h_1 + h_2)} \\ c_2 = \sqrt{\varepsilon g \frac{h_1 h_2}{h_1 + h_2}} \end{cases} \quad (2.11)$$

are the barotropic and baroclinic phase speeds respectively. Referring to equation (2.8), the two corresponding solutions for Z_2 are:

$${}^i Z_2 = \left(1 - \frac{g h_1}{c_i^2}\right) {}^i Z_1 \quad i=1,2 \quad (2.12)$$

Thus the expansion of Z_i in terms of the eigenmodes ${}^j Z_i$ requires the ratios:

$$\lambda_i = \frac{{}^i Z_1}{{}^i Z_2} = \frac{1}{1 - \frac{g h_1}{c_i^2}} \quad i=1,2$$

Thus the general solutions can be written as:

$$\left\{ \begin{array}{l} Z_1 = \lambda_1 F e^{\sqrt{p^2+f^2} \frac{y}{c_1}} + \lambda_2 G e^{\sqrt{p^2+f^2} \frac{y}{c_2}} + \\ \lambda_1 F' e^{-\sqrt{p^2+f^2} \frac{y}{c_1}} + \lambda_2 G' e^{-\sqrt{p^2+f^2} \frac{y}{c_2}} \\ Z_2 = F e^{\sqrt{p^2+f^2} \frac{y}{c_1}} + G e^{\sqrt{p^2+f^2} \frac{y}{c_2}} + \\ F' e^{-\sqrt{p^2+f^2} \frac{y}{c_1}} + G' e^{-\sqrt{p^2+f^2} \frac{y}{c_2}} \end{array} \right.$$

where the constants F , F' , G and G' are determined from the coastal boundary conditions. However, due to the channel symmetry with respect to the x axis (Figure 2.1), it is easily shown that:

$$\left\{ \begin{array}{l} Z_1(p, y) = 2 \lambda_1 F \sinh\left(\sqrt{p^2+f^2} \frac{y}{c_1}\right) + 2 \lambda_2 G \sinh\left(\sqrt{p^2+f^2} \frac{y}{c_2}\right) \\ Z_2(p, y) = 2 F \sinh\left(\sqrt{p^2+f^2} \frac{y}{c_1}\right) + 2 G \sinh\left(\sqrt{p^2+f^2} \frac{y}{c_2}\right) \end{array} \right. \quad (2.13)$$

From equations (2.6) and (2.7):

$$\left\{ \begin{array}{l} (p^2+f^2) V_1 = -gp Z_{1,y} - f \frac{T}{\rho_1 h_1} \\ (p^2+f^2) V_2 = -gp [\varepsilon Z_{2,y} + (1-\varepsilon) Z_{1,y}] \end{array} \right. \quad (2.14)$$

so that, by setting $V_1=0$ and $V_2=0$ at the coast, equation

2.14 becomes:

$$\left\{ \begin{array}{l} Z_{1,y}|_{(y-a)} = \frac{-f}{g h_1 \rho_1} \frac{T}{p} \\ (\varepsilon Z_{2,y} + (1-\varepsilon) Z_{1,y})|_{(y-a)} = 0 \end{array} \right.$$

Thus, it is then readily shown that:

$$\left\{ \begin{array}{l} F = \frac{-f}{2 g h_1 \rho_1} \frac{\Lambda_2 c_1}{\Delta} \frac{T}{p \sqrt{p^2 + f^2} \cosh\left(\sqrt{p^2 + f^2} \frac{a}{c_1}\right)} \\ G = \frac{f}{2 g h_1 \rho_1} \frac{\Lambda_1 c_2}{\Delta} \frac{T}{p \sqrt{p^2 + f^2} \cosh\left(\sqrt{p^2 + f^2} \frac{a}{c_2}\right)} \end{array} \right. \quad (2.15)$$

where $\Lambda_i = \varepsilon + (1-\varepsilon)\lambda_i$, ($i=1,2$) and $\Delta = \lambda_1 \Lambda_2 - \lambda_2 \Lambda_1$.

At last, the Z expressions appear as:

$$\left\{ \begin{array}{l} Z_1 = \frac{-f}{g h_1 \rho_1} \frac{T}{p \sqrt{p^2 + f^2}} \left\{ \frac{\Lambda_2 \lambda_1 c_1}{\Delta} \Psi_1 - \frac{\Lambda_1 \lambda_2 c_2}{\Delta} \Psi_2 \right\} \\ Z_2 = \frac{-f}{g h_1 \rho_1} \frac{T}{p \sqrt{p^2 + f^2}} \left\{ \frac{\Lambda_2 c_1}{\Delta} \Psi_1 - \frac{\Lambda_1 c_2}{\Delta} \Psi_2 \right\} \end{array} \right. \quad (2.16)$$

where the functions $\Psi_i(p,y)$ are defined as:

$$\Psi_i(p, y) = \frac{\sinh\left(\sqrt{p^2+f^2} \frac{y}{c_i}\right)}{\cosh\left(\sqrt{p^2+f^2} \frac{a}{c_i}\right)} \quad i=1,2 \quad (2.17)$$

The average velocity expressions are computed from the y derivatives of Z_1 and Z_2 (equations 2.6 and 2.7). After setting:

$$\Phi_i(p, y) = \frac{\cosh\left(\sqrt{p^2+f^2} \frac{y}{c_i}\right)}{\cosh\left(\sqrt{p^2+f^2} \frac{a}{c_i}\right)} \quad i=1,2 \quad (2.18)$$

they appear as:

$$\left\{ \begin{aligned} U_1 &= \frac{f^2}{\rho_1 h_1} \frac{T}{p(p^2+f^2)} \left\{ \frac{\Lambda_2 \lambda_1}{\Delta} \Phi_1 - \frac{\Lambda_1 \lambda_2}{\Delta} \Phi_2 \right\} + \frac{1}{\rho_1 h_1} \frac{pT}{p^2+f^2} \\ V_1 &= \frac{f}{\rho_1 h_1} \frac{T}{p^2+f^2} \left\{ \frac{\Lambda_2 \lambda_1}{\Delta} \Phi_1 - \frac{\Lambda_1 \lambda_2}{\Delta} \Phi_2 \right\} - \frac{f}{\rho_1 h_1} \frac{T}{p^2+f^2} \end{aligned} \right. \quad (2.19)$$

$$\left\{ \begin{aligned} U_2 &= \frac{f^2}{\rho_1 h_1} \frac{\Lambda_2 \lambda_1}{\Delta} \frac{T}{p(p^2+f^2)} (\Phi_1 - \Phi_2) \\ V_2 &= \frac{f}{\rho_1 h_1} \frac{\Lambda_2 \lambda_1}{\Delta} \frac{T}{p^2+f^2} (\Phi_1 - \Phi_2) \end{aligned} \right. \quad (2.20)$$

Equations (2.16), (2.19) and (2.20) describe the total Laplace Transform solution to order ε for any spatially

uniform wind stress distribution (T). To obtain an aperiodic response, the wind stress function $\tau(t)$ has to be slowly varied in time so that the Inverse Transforms of these equations do not produce only the strong transient wave-like response.

2.2.4. Longshore steady wind forcing

Much of the information of the physical mechanism involving a Coastal Jet subject to wind forcing rises from the most idealized wind setting (Csanady, 1977). Thus, let a wind directed parallel to the coast, constant in space and in time for $t > 0$. Since the absence of bottom friction is only justifiable before significant velocities develop, the model describes only the initiation of motion.

The Laplace Transform of $\tau(t) = \tau_0 \mu(t)$ being simply τ_0/p , the singularities of the functions $U_i(p, y)$, $V_i(p, y)$ and $Z_i(p, y)$ lie at $p=0$ and $p = \pm if$ (Equations 2.16, 2.19 and 2.20). The only possible non-wavelike contribution arises from the singular point at $p=0$ which is a simple pole in expressions for $V_i(p, y)$ and a second order pole for all others. This fact allows the calculation of the response functions through the Residue Theorem.

The Inverse Laplace Transform of a function $g(p)$ equals the sum of the residues of $g(p)e^{pt}$ at the poles of $g(p)$. The residue for a pole p_0 of order n is given by:

$$\text{Residue } (p_0) = \lim_{p \rightarrow p_0} \frac{1}{(n-1)!} \frac{d^{(n-1)}}{dp^{(n-1)}} \left[(p-p_0)^n e^{pt} g(p) \right]$$

where d^{n-1}/dp^{n-1} represents the (n-1)th derivative with respect to the Laplace variable p.

The steady wind aperiodic response for the surface layer then appears as:

$$\left\{ \begin{array}{l} u_1(t, y) = \frac{\tau_0 t}{\rho_1 h_1} \left\{ \frac{\lambda_2 \lambda_1}{\Delta} \frac{\cosh\left(\frac{y}{R_1}\right)}{\cosh\left(\frac{a}{R_1}\right)} - \frac{\lambda_1 \lambda_2}{\Delta} \frac{\cosh\left(\frac{y}{R_2}\right)}{\cosh\left(\frac{a}{R_2}\right)} \right\} \\ v_1(t, y) = \frac{\tau_0}{f \rho_1 h_1} \left\{ \frac{\lambda_2 \lambda_1}{\Delta} \frac{\cosh\left(\frac{y}{R_1}\right)}{\cosh\left(\frac{a}{R_1}\right)} - \frac{\lambda_1 \lambda_2}{\Delta} \frac{\cosh\left(\frac{y}{R_2}\right)}{\cosh\left(\frac{a}{R_2}\right)} \right\} - \frac{\tau_0}{f \rho_1 h_1} \\ \zeta_1(t, y) = \frac{-\tau_0 t}{g h_1 \rho_1} \left\{ \frac{\lambda_2 \lambda_1 c_1}{\Delta} \frac{\sinh\left(\frac{y}{R_1}\right)}{\cosh\left(\frac{a}{R_1}\right)} - \frac{\lambda_1 \lambda_2 c_2}{\Delta} \frac{\sinh\left(\frac{y}{R_2}\right)}{\cosh\left(\frac{a}{R_2}\right)} \right\} \end{array} \right. \quad (2.21)$$

while for the bottom layer, it is:

$$\left\{ \begin{array}{l}
u_2(t, y) = \frac{\tau_0 t}{\rho_1 h_1} \frac{\Lambda_1 \Lambda_2}{\Delta} \left\{ \frac{\cosh\left(\frac{y}{R_1}\right)}{\cosh\left(\frac{a}{R_1}\right)} - \frac{\cosh\left(\frac{y}{R_2}\right)}{\cosh\left(\frac{a}{R_2}\right)} \right\} \\
v_2(t, y) = \frac{\tau_0}{\rho_1 h_1 f} \frac{\Lambda_1 \Lambda_2}{\Delta} \left\{ \frac{\cosh\left(\frac{y}{R_1}\right)}{\cosh\left(\frac{a}{R_1}\right)} - \frac{\cosh\left(\frac{y}{R_2}\right)}{\cosh\left(\frac{a}{R_2}\right)} \right\} \\
\zeta_2(t, y) = \frac{-\tau_0 t}{g h_1 \rho_1} \left\{ \frac{\Lambda_2 c_1}{\Delta} \frac{\sinh\left(\frac{y}{R_1}\right)}{\cosh\left(\frac{a}{R_1}\right)} - \frac{\Lambda_1 c_2}{\Delta} \frac{\sinh\left(\frac{y}{R_2}\right)}{\cosh\left(\frac{a}{R_2}\right)} \right\}
\end{array} \right. \quad (2.22)$$

The distances R_1 and R_2 are surface and internal radii of deformation characterizing respectively the barotropic and baroclinic decay scales of the coastal jets generated at each shore:

$$R_1 = \frac{c_1}{f} \qquad R_2 = \frac{c_2}{f}$$

2.3. Discussion

Although highly idealized, this conceptual model still allows great insight into the wind-forced flow dynamics. The solution is proportional to time, thus for short time scales, the aperiodic part of the longstrait average velocities and of the seasurface and interface grow linearly in time until the friction (which is function of the average

velocities) becomes big enough so that friction would remove part of the momentum and consequently makes the channel jet equations invalid. This comes from the fact that a steady wind is a continuous "source" of momentum, and the two-layer model, as described by equations (2.2), does not contain any "sink" term to remove momentum. The inviscid dynamics leads eventually to unbounded alongshore transports.

For each position across the channel, the cross-channel aperiodic average velocities appear as constants in time. Their wave-like part (not shown here) is opposite in sign to the aperiodic solution such that v_1 and v_2 satisfy the initial condition ($v_1=0$ and $v_2=0$ at $t=0$). The seasurface distortion exhibits a fluid transfer from south to north, due to the action of Coriolis force. This in turn has to be compensated by a transfer in the opposite direction in the lower layer, because of continuity, generating then a cross-shore flow in the lower layer. The Coriolis force distributes the momentum to the longstrait flow and generates a lower layer longshore average flow via geostrophic adjustment.

For a hypothetical channel width much larger than R_2 , the two facing jets would diminish considerably before reaching each other, and the channel response would consist of two distinct jets trapped to the opposing shores (dotted lines in Figure 2.2). The seasurface rises and falls respectively at the northern and southern shores leaving a

large portion of the channel free of net vertical transport. Hence, over most of the channel, the wind momentum is evenly distributed over the entire depth H , since it is outside the baroclinic decay length scale.

Within the coastal boundary layers, the cross-channel transports are negligible while the upper layer exhibits the largest longshore flow and the lower layer, the smallest flow. Very close to the coast:

$$\begin{aligned} u_1 &= \frac{\tau_0 t}{\rho_1 h_1} & u_2 &= 0 \\ v_1 &= 0 & v_2 &= 0 \end{aligned}$$

In other words, the wind stress momentum input is distributed over the upper layer only. In the absence of friction and of long channel pressure gradients, the presence of the coast imposes a zero cross-shore flow, thus eliminating the generation of longshore flow in the lower layer via 'adjustment drift' (Csanady, 1982).

The first of Equations (2.4) describes the way the wind input momentum is distributed between long-shore acceleration and Coriolis force. The model response shows that the Ekman average velocity term $\tau_0/(f\rho_1 h_1)$ is entirely carried out by the upper layer cross-shore velocity (Equation 2.21). In a frictionless two-layer flow, Ekman spiral is confined to the upper layer regardless of depths

since there is no stress transfer to the bottom layer.

In the case of Gibraltar Strait, the channel width (2a) is approximately equal to the internal Rossby radius R_2 . This means that the 'Gibraltar channel' response consists of two opposing jets superposed such that they overlap enough so that there is no "free" space for a simple Ekman drift between jets.

Figure 2.2 presents the seasurface and interface elevations drawn for two channel widths versus the normalized cross-shore position y ($-1 < y < 1$). The seasurface plot shows that effectively the wind drags water in the upper layer such as the Coriolis force (first equation 2.4) generates a cross-shore response to the right of the channel axis. The gravity balance disequilibrium that results is then restored by the interface. After approximately 5 hours of constant wind, the magnitude of this water piling is of the order of 3 cm at the northern coast (and 3 cm depression on the opposing side). Because of the small density defect (equation 2.3), a comparatively strong displacement (10 m) of the thermocline is needed to restore the gravity balance.

For density defect (equation 2.3) corresponding to the strong stratification observed in the Strait of Gibraltar, the barotropic and baroclinic phase speeds are approximately 76.7 ms^{-1} and 1.2 ms^{-1} respectively and their associated length scales $R_1=900 \text{ km}$ and $R_2=14.5 \text{ km}$. Note that the baroclinic Rossby radius, which is the smallest, is almost

equal to the channel width ($2a=15$ km). Figure 2.2 presents the seafloor and interface like two solid plates, tilting proportionally to time. This fact comes from the equality $2a=R_2$ which constrains the argument of the internal mode function y/R_2 to lie within the interval $-1/2 < y/R_2 < 1/2$, thus making the hyperbolic sine function behave like its first order expansion term y/R_2 . This approximation is even better for the external mode hyperbolic sine function since its argument is restrained to a much narrower interval $|y/R_1| < 0.008$.

An estimate of the wind-driven longshore velocity can be determined using the gain factor between wind and current computed in chapter 1 and typical values of τ . Since the average gain factor evaluated at TN is approximately $0.6 \text{ ms}^{-1}/\text{Pa}$, a wind of 0.8 Pa creates a current of 0.48 ms^{-1} . Although this value is grossly exaggerated, the channel jet solution reaches such magnitude for the longshore average velocity for a time length on the order of 15 hours.

As successful as this model is in illuminating the dynamics of the initial response of the strait to wind driving, the lack of dissipation prevents it from helping us understand the longer term behavior of the strait under wind driving. These shortcomings are addressed in the next section.

Table 2.1: Typical data of Gibraltar Strait channel jet

Upper layer depth h_1	100 m
Lower layer depth h_2	500 m
Channel half width a	7500 m
Upper layer density ρ_1	1023 kgm^{-3}
Density defect ε	$1.9 \cdot 10^{-3}$
Coriolis Parameter f	$8.57 \cdot 10^{-5} \text{ s}^{-1}$
Gravity g	9.81 ms^{-2}
Wind speed u_w (Levantine)	20 ms^{-1}
Wind stress τ	0.3 Pa
External Rossby radius R_1	900 km
External phase speed c_1	76.7 ms^{-1}
Internal Rossby radius R_2	14.5 km
Internal phase speed c_2	1.2 ms^{-1}

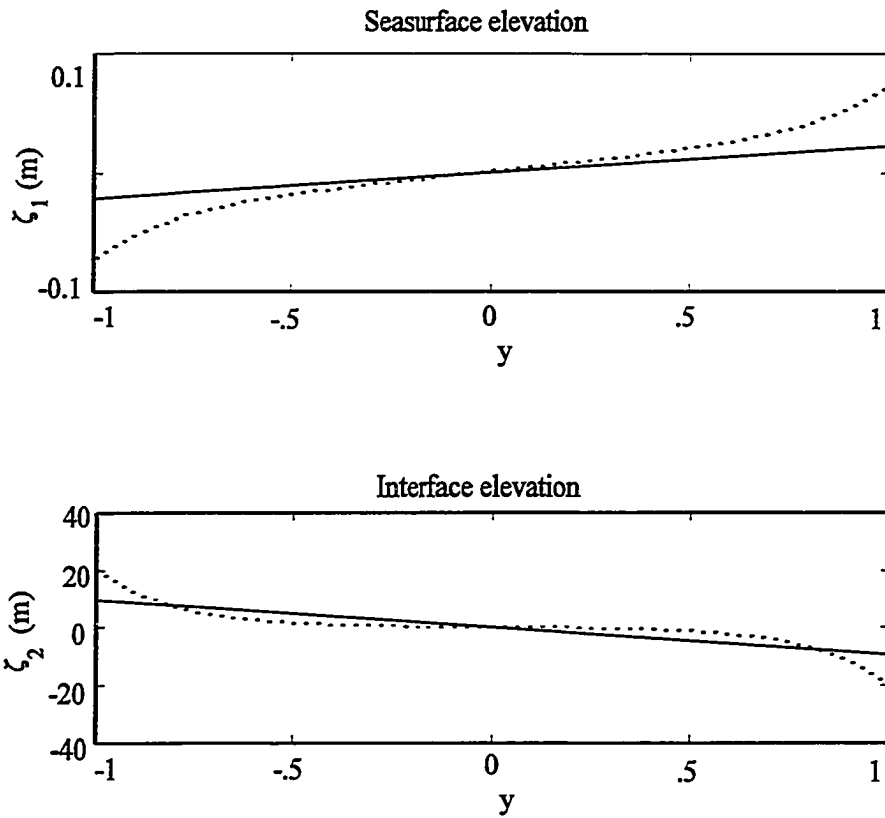


Figure 2.2: Seasurface and interface elevations versus a normalized cross section position. The elevations are for a 15 km (solid line) and 150 km (dotted line) channel width.

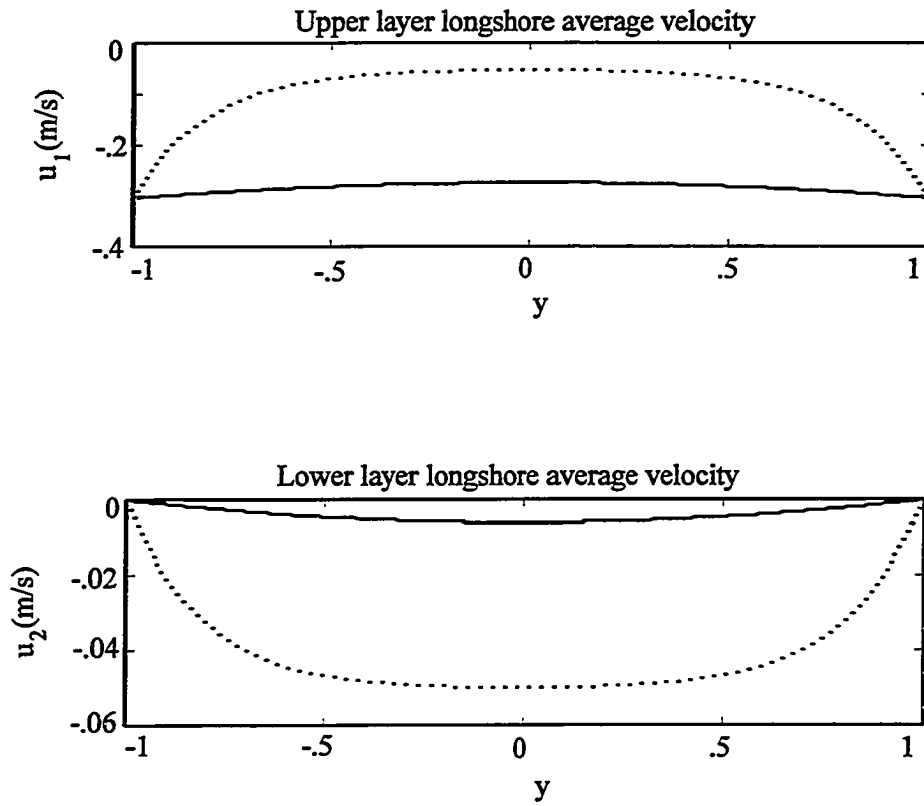


Figure 2.3: Longchannel average velocities versus the normalized cross section position. Results for a 15 km (solid line) and 150 km (dotted line) wide channel are presented.

CHAPTER 3

Frictional adjustment numerical model

3.1. Governing equations

As defined in the previous model, a two-layer channel flow is considered. The bottom layer (mean depth h_2) is bounded on the top by the pycnocline the deformation of which is measured by the elevation ζ_2 . The upper layer (mean depth h_1) is delimited by the seasurface elevation ζ_1 and the interface elevation ζ_2 (Figure 2.1). The governing linearized momentum and continuity equations are:

$$\left\{ \begin{array}{l} \bar{u}_{1,t} + 2\bar{\Omega} \times \bar{u}_1 - g \bar{\nabla} \zeta_1 + \frac{\bar{\tau} - \bar{\tau}_i}{\rho_1 h_1} \\ \nabla \cdot \bar{u}_1 = \frac{1}{h_1} (\zeta_{2,t} - \zeta_{1,t}) \\ \bar{u}_{2,t} + 2\bar{\Omega} \times \bar{u}_2 - g \bar{\nabla} [(1-\varepsilon) \zeta_1 + \varepsilon \zeta_2] + \frac{\bar{\tau}_i - \bar{\tau}_b}{\rho_2 h_2} \\ \nabla \cdot \bar{u}_2 = - \frac{1}{h_2} \zeta_{2,t} \end{array} \right. \quad (3.1)$$

where u_i is the i -th layer-averaged velocity, τ , τ_i and τ_b represent the wind stress, the interfacial stress and the bottom stress respectively. The channel is considered infinitely long such that the longchannel pressure gradients

are omitted and that all $\partial/\partial x$ partial derivatives vanish. The coastal constraints stipulate that there is no flow through the solid boundaries in either layer: $v_1=0$ and $v_2=0$ at $y=-a$ and $y=a$. Since the magnitude of the cross-shore average velocities are expected to be small compared to those along the channel, the interfacial and bottom stress terms in the y direction are neglected. If the interfacial and bottom stresses in the x direction are parameterized by means of linear drag laws, then the full set of equations become:

$$\begin{cases} u_{1,t} - f v_1 - \frac{\tau}{\rho_1 h_1} - C_i (u_1 - u_2) \\ v_{1,t} + f u_1 - g \zeta_{1,y} \\ h_1 v_{1,y} - \zeta_{2,t} - \zeta_{1,t} \end{cases} \quad (3.2)$$

$$\begin{cases} u_{2,t} - f v_2 - C_i (u_1 - u_2) - C_b u_2 \\ v_{2,t} + f u_2 - g [\varepsilon \zeta_{2,y} + (1 - \varepsilon) \zeta_{1,y}] \\ h_2 v_{2,y} - \zeta_{2,t} \end{cases} \quad (3.3)$$

where the interfacial stress depends linearly on the velocity difference between the two layers. The momentum and continuity equations (3.2 and 3.3) are now coupled through the cross-shore pressure gradient terms, as well as through

the longshore average velocities.

3.2. Analytical steady state solution

This solution, represented with overbars, characterizes the asymptotic behavior of the average flow after all transient wind effects have disappeared. After omitting the time derivatives, the continuity equations (last equations in 3.1 and 3.2) require that cross-shore steady state average velocities be constant in y . Thus the cross-shore average velocities are zero because of no flow lateral boundary conditions. The longshore momentum equations (first equations of 3.1 and 3.2) become a balance between the stress terms acting on each layer while the cross-channel momentum equations are geostrophic. The steady solutions are:

$$\left\{ \begin{array}{l} \overline{u}_1(y) = \left(\frac{1}{C_i} + \frac{1}{C_b} \right) \frac{\tau}{\rho_1 h_1} \\ \overline{v}_1(y) = 0 \\ \overline{\zeta}_1(y) = -\frac{f}{g} \left(\frac{1}{C_i} + \frac{1}{C_b} \right) \frac{\tau}{\rho_1 h_1} y \end{array} \right. \quad (3.5)$$

$$\left\{ \begin{array}{l} \overline{u}_2(y) = \frac{1}{Cb} \frac{\tau}{\rho_1 h_1} \\ \overline{v}_2(y) = 0 \\ \overline{\zeta}_2(y) = -\frac{f}{g\varepsilon} \left\{ \frac{1}{Cb} - (1-\varepsilon) \left(\frac{1}{Ci} + \frac{1}{Cb} \right) \right\} \frac{\tau}{\rho_1 h_1} y \end{array} \right. \quad (3.6)$$

The solutions given in equations 3.5 and 3.6 show that the steady state channel response is extremely simple. The cross channel flow disappears entirely in both layers, and the along-channel flow is slab-like and devoid of cross-channel variations. The ratio of upper to lower layer longshore flows is controlled by the interfacial and bottom drag coefficients and is given by:

$$\frac{\overline{u}_1(y)}{\overline{u}_2(y)} = \frac{Cb + Ci}{Ci}$$

In the limit $Cb \approx Ci$ and the ratio is 2. For a more realistic case where $Ci \ll Cb$, the predominance of the upper layer currents would be much more pronounced and the ratio would be approximately Cb/Ci .

Because of the geostrophic cross-shore balance, the constant currents are associated with constant seasurface and interface slopes. To the first order of ε , the interfacial slope may be expressed approximately in terms of the seasurface slope as:

$$\frac{\frac{\partial \bar{\zeta}_1(y)}{\partial y}}{\frac{\partial \bar{\zeta}_2(y)}{\partial y}} = \frac{\bar{\zeta}_1(y)}{\bar{\zeta}_2(y)} \approx \varepsilon \frac{C_i + C_b}{C_b}$$

As expected, the interface slopes in the opposite direction as the searface, and has a much larger magnitude.

In view of the characteristic shore-trapped structure of the channel jet solution of the previous chapter, the slab flow seen in the steady state frictional model is at first a startling result. It says that, in the presence of friction, the channel jet structure is a transient feature.

An obvious question arises: how do the 'S' shaped surface and interface displacements and the exponentially decaying longshore velocities evolve into the slablike flow of the frictional steady state model? This intriguing question can be answered by careful consideration of the evolution of the dynamic balances. In the following section, a numerical model of the time-dependent frictional flow is presented in order to help elucidate the process by which the paired channel jets evolve into a slab flow.

3.3. Numerical model

Time-dependent solutions of the average velocity equations (3.1 to 3.4) are not obtained by standard analytical techniques, so a discrete numerical solution is sought. A staggered space-time grid (Greenspan, 1974) is

used to expand the solution in the cross-shore direction and in time between the initial condition and the steady state solution (Figure 3.1). The cross-channel grid size Δy is obtained by subdividing the channel width ($0 < y < 2a$) into N_y equal parts. However, since the boundary conditions apply only to the cross shore velocities, the first row of grid points from the two coasts ($j=1$ and $j=N_y-1$) contain only the four unknowns (u_i, ζ_i). Thus, the space grid size must be an even integer. The time scale spans over N_t intervals of length Δt .

At grid points where the couples (u_i, ζ_i) are to be determined (Figure 3.1), the second order derivative scheme allows the longshore momentum and continuity equations to become for the upper layer:

$$\begin{aligned} & \frac{(u_1)_{i-1,j} - (u_1)_{i+1,j}}{2\Delta t} - f \frac{(v_1)_{i,j-1} + (v_1)_{i,j+1}}{2} \\ & + Ci (u_1)_{i,j} - Ci (u_2)_{i,j} - \frac{\tau}{\rho_1 h_1} \\ & \frac{(v_1)_{i,j-1} - (v_1)_{i,j+1}}{2\Delta y} \\ & + \frac{1}{h_1} \frac{(\zeta_1)_{i-1,j} - (\zeta_1)_{i+1,j}}{2\Delta t} - \frac{1}{h_1} \frac{(\zeta_2)_{i-1,j} - (\zeta_2)_{i+1,j}}{2\Delta t} = 0 \end{aligned}$$

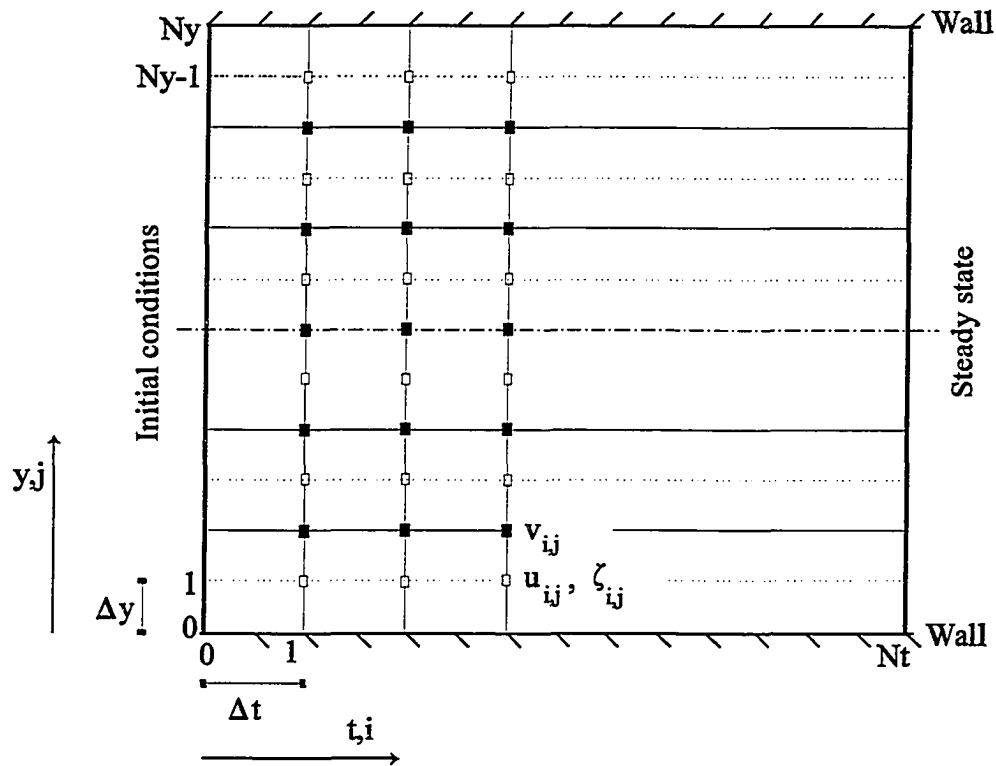


Figure 3.1: Staggered space-time grid for numerical model. At filled square grid points, the 2 cross-shore average velocities v_1 and v_2 are unknown, and similarly at empty grid points u_1 , u_2 , ζ_1 and ζ_2 are to be determined.

For the bottom layer:

$$\frac{(u_2)_{i-1,j} - (u_2)_{i-1,j}}{2\Delta t} - f \frac{(v_2)_{i,j-1} + (v_2)_{i,j-1}}{2}$$

$$- C_i (u_1)_{i,j} + (C_i + C_b) (u_2)_{i,j} = 0$$

$$\frac{(v_2)_{i,j-1} - (v_2)_{i,j-1}}{2\Delta y} + \frac{1}{h_2} \frac{(\zeta_2)_{i-1,j} - (\zeta_2)_{i-1,j}}{2\Delta t} = 0$$

Similarly, at points where v_i are unknown, the cross-shore momentum equations are now:

$$\frac{(v_1)_{i-1,j} - (v_1)_{i-1,j}}{2\Delta t} + f \frac{(u_1)_{i,j-1} + (u_1)_{i,j-1}}{2}$$

$$+ g \frac{(\zeta_1)_{i,j-1} - (\zeta_1)_{i,j-1}}{2\Delta y} = 0$$

$$\frac{(v_2)_{i-1,j} - (v_2)_{i-1,j}}{2\Delta t} + f \frac{(u_2)_{i,j-1} + (u_2)_{i,j-1}}{2}$$

$$+ g \left(\varepsilon \frac{(\zeta_2)_{i,j-1} - (\zeta_2)_{i,j-1}}{2\Delta y} + (1 - \varepsilon) \frac{(\zeta_2)_{i,j-1} - (\zeta_2)_{i,j-1}}{2\Delta y} \right) = 0$$

The finite-difference approximation of the system of partial differential equations (Equations 3.2 and 3.3) is reduced to a linear algebraic system of the form $A.X=B$ where A is the

square matrix of finite difference coefficients multiplying the unknown column vector X built of the six discretized functions u_i , v_i and ζ_i , and B the forcing column vector containing the boundary, initial and steady state conditions. The solution of such a system is computed by Gaussian elimination with partial pivoting (LINPACK routine in Matlab software). For values of N_t and N_y suitable to describe the space-time behavior of the channel solution with some accuracy, the size of A ($3N_yN_t+N_y$) becomes quickly such a great number that any increase of the grid dimensions affects greatly the convergence of the solution if not the whole computation of A^{-1} . An arbitrary choice for N_y is 11, to allow somewhat of a large range for N_t (10 to 20) and still allow the computation of A^{-1} .

3.3.1. Choice of parameters

The literature suggests values for the averaged velocity bottom drag coefficient C_b ranging between 0.0005 to 0.005 s^{-1} (Jenter and Madsen, 1989; Poon and Madsen, 1991; Csanady, 1982). Based on the choice $C_b=0.005 \text{ s}^{-1}$, the interfacial drag coefficient C_i can be estimated from the statistical analysis of chapter 1. If the station TN (depth 120 m) is taken to contain the upper layer only, Figure 1.6 shows that, for a period between 3.75 days and 7 days, the autospectral values of the EOF mode 1 along-channel velocity are approximately 6 and $10.5 (\text{ms}^{-1})^2 \text{ cph}^{-1}$. These are

estimates of the kinetic energy per unit frequency for the depth-averaged flow and lead to an average root-mean-square velocity of the order of 0.36 ms^{-1} . Reporting this value to a steady state along strait average velocity (first of Equation 3.5) leads to $C_i \approx 2.6 \cdot 10^{-5} \text{ s}^{-1}$. However, this value does not take into account the fact that the wind forces only about 50% of the current variance, the ordinary coherence for the same frequency band being equal to 0.7 (Figure 1.7 and 1.8). Thus, a more appropriate value of C_i is $5 \cdot 10^{-5} \text{ s}^{-1}$.

A conventional procedure to solve partial differential equations begins with the assumption that the variables are separable (as applied in the previous chapter). This technique does not produce a solution for the analytical friction model, because space and time behavior of the currents are not separable. That is, the time scale of frictional adjustment is dependant on cross-channel position, and similarly, the cross-channel structure depends upon time.

However, one can estimate the time scale required for the interfacial friction term to be of the same order as the local acceleration in the upper layer. This intermediate time scale is given by C_i^{-1} , or 6 hours. In reality, the wind stress momentum is distributed between local acceleration, interfacial stress and rotation. Because of the complexity of the problem, and in the absence of an

analytical solution, the numerical model remains the only reliable way to estimate a time of frictional adjustment defined as the asymptotic approach to the steady state solution.

3.3.2. Model results and discussion

Results of the numerical model are presented for channel widths of $10R_2$ and R_2 (Gibraltar Strait width). Each numerical trial generates matrices of six functions u_i , v_i , ζ_i ($i=1,2$) where the rows and columns represent respectively the cross-channel positions and the elapsed time from the initial to the steady state. The computations are executed for time increment values Δt large enough to provide little wave-like oscillations of the six functions. After numerical experiments, Δt was set to 6 hours, a compromise between short time steps and number of time steps.

Figures 3.2 and 3.3 show the solution evolution in time both near shore and along the central axis of two functions u_1 and ζ_2 , chosen for their comparatively large magnitudes. Figures 3.4 and 3.5 present the 6 numerical model distributions for the two channel width considered (R_2 and $10R_2$).

The results of the numerical model show clearly that, as anticipated, the channel jet solution is a valid approximation to the dynamics for an initial period during which the currents accelerate without much modification by

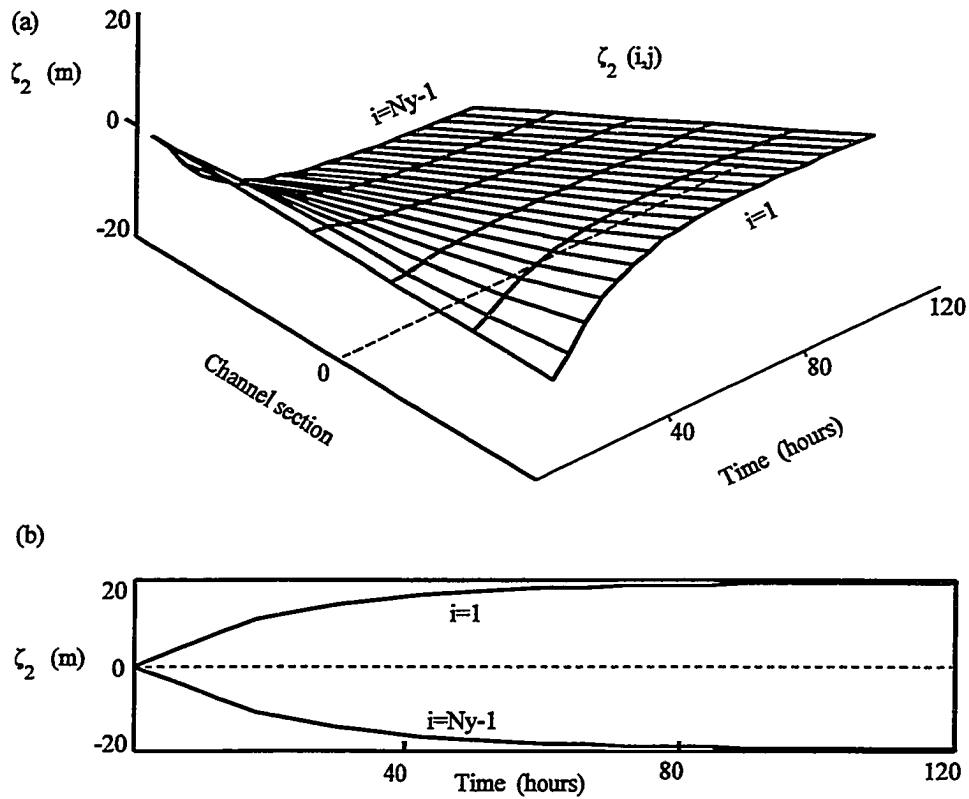


Figure 3.2: Interface elevation space-time distribution computed for a channel width of $10R_2$ (150 km): (a) 3D view of the discretized matrix $\zeta_2(i,j)$ where i and j represent the index for space steps and time steps respectively; (b) closest to shores $i=1$ and $i=N_y-1$ time profiles of ζ_2 . In both plots, the profile in dashed line is interpolated along the channel axis ($y=0$).

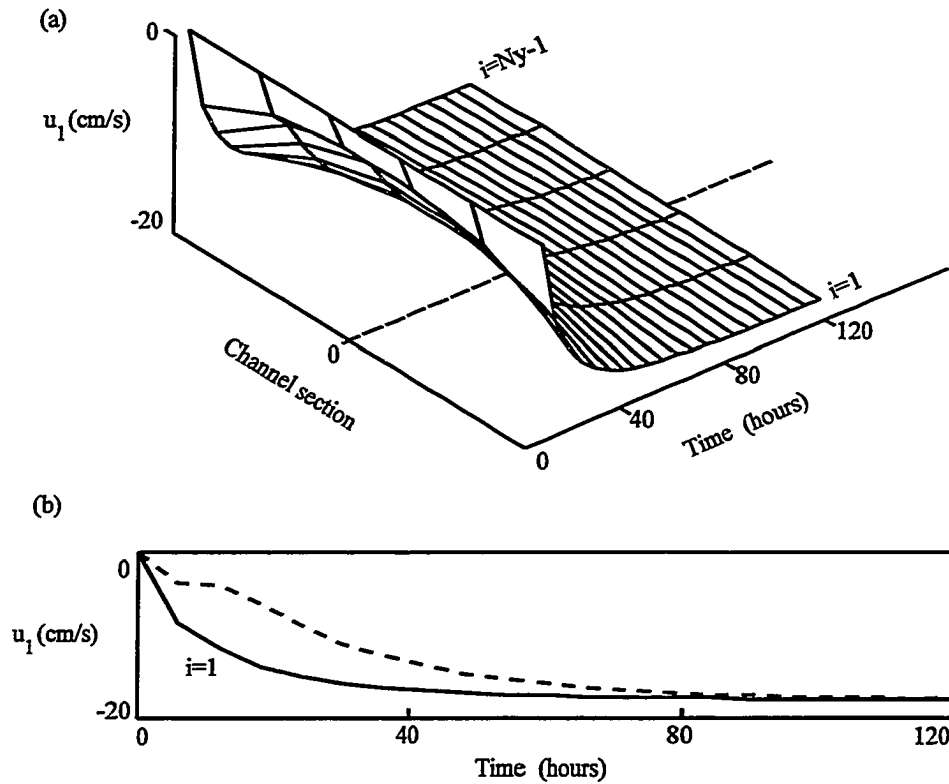


Figure 3.3: Long-channel upper layer averaged velocity space-time distribution computed for a channel width of $10R_2$ (150 km): (a) 3D view of the discretized matrix $u_1(i, j)$ where i and j represent the index for space steps and time steps respectively; (b) closest to shores $i=1$ profile vs time. Since the velocity distribution is symmetric with respect to the channel axis, only this plot is shown. In both plots, the profile in dashed line is interpolated for the channel axis ($y=0$).

interfacial and bottom friction. After approximately one time step (6 hours for a channel width of $10R_2=150$ km), dissipation has become important and the numerical circulation shows reduced local acceleration of the currents and pressure gradient fields. With the linear friction coefficients chosen for this study, currents are approximately half what they are in the channel jet model. These results show that, as suggested by Csanady (1977), the linear inviscid dynamics are adequate to qualitatively describe the processes of wind-driven current generation in the presence of coastal constraints. However, after the wind has been acting for longer periods, the fundamental nature of the coastal regions response begin to change.

The nature of this change is most clearly seen and understood for a wide channel ($R_2 \ll 2a$). Since after the onset of wind-stress forcing, the currents near the coasts grow more rapidly, they first achieve magnitudes large enough for the dissipation terms to balance the momentum input by the wind. As a result, the near-shore regions first reach steady state frictional equilibrium. When this occurs, all of the wind stress momentum is directly dissipated, in effect 'short circuiting' the momentum equations. As a result, at these locations no further downwind acceleration occurs, and there is no longer Ekman transport. Thus the cross-shore currents reduce to zero and the alongshore current and cross-shore pressure gradient have reached their final

(steady state) values.

Farther from the coasts, current continue to grow under the influence of the wind, and cross-shore flow (though reduced), is still taking place. It is as if the coastal constraints has been imposed seaward of the actual coast. The cross flow in regions not yet at steady state acts to transfer mass across channel and moves sealevel and interface elevation toward their linear steady state distributions.

In summary, we see that the steady state occurs first at the coasts, and as time goes on, the steady state spreads toward the center of the channel. Steady state occurs when the coastal constraint on cross flow hold for the whole channel. At this time, the along channel velocities are uniform (slab-like), the seasurface and interface have constant across channel slopes, and cross flow is zero. These results have allowed us to bridge our understanding of the evolution of wind-driven flow in a channel between the initial coastal jet dynamics and the final steady state.

The principal findings are that the fundamental structure of the current changes as frictional effects become dominant. The characteristic coastal trapping and linear temporal growth of along channel current and sea level and interface deformations give way progressively to a slab flow in each of the two layers. Thus we see that the channel jet is an ephemeral phenomenon that cannot long

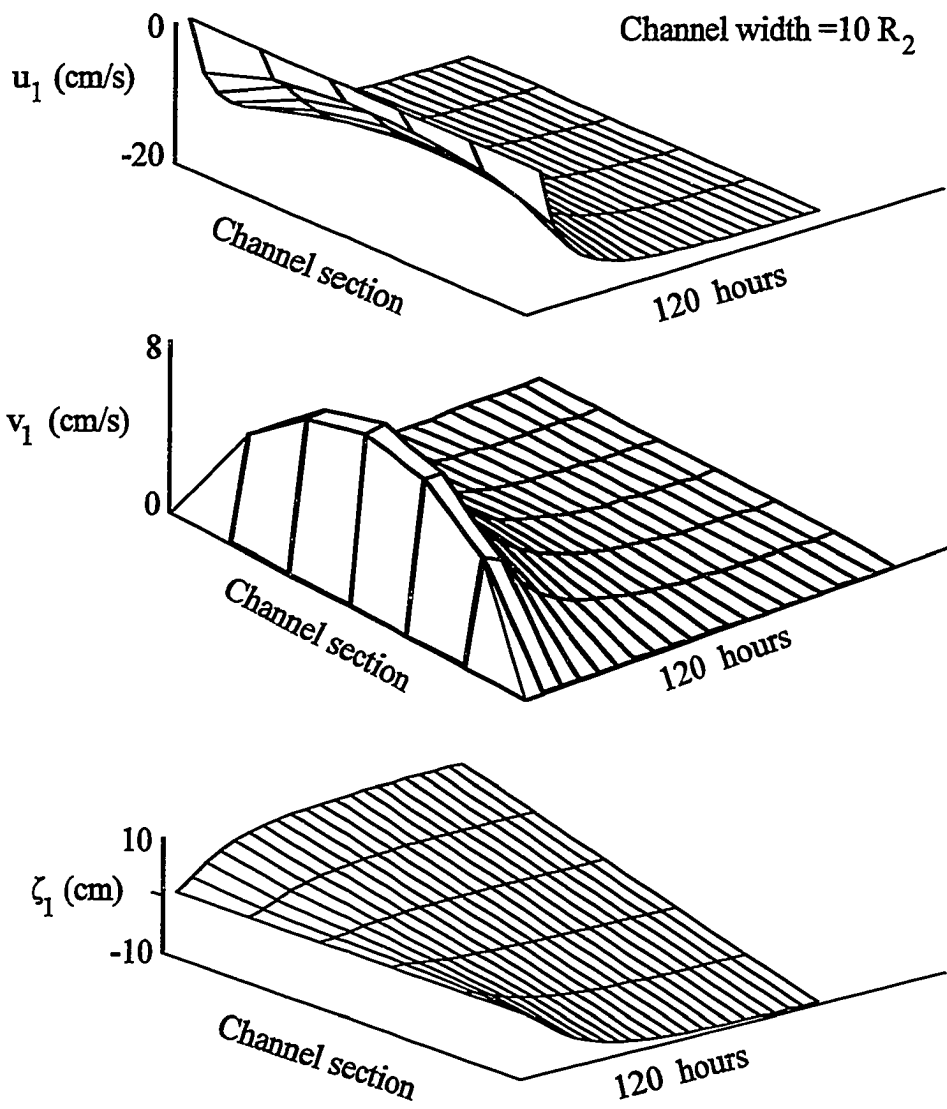


Figure 3.4: Space-time distributions of the channel flow upper layer components for a channel width of $10R_2$ (150 km).

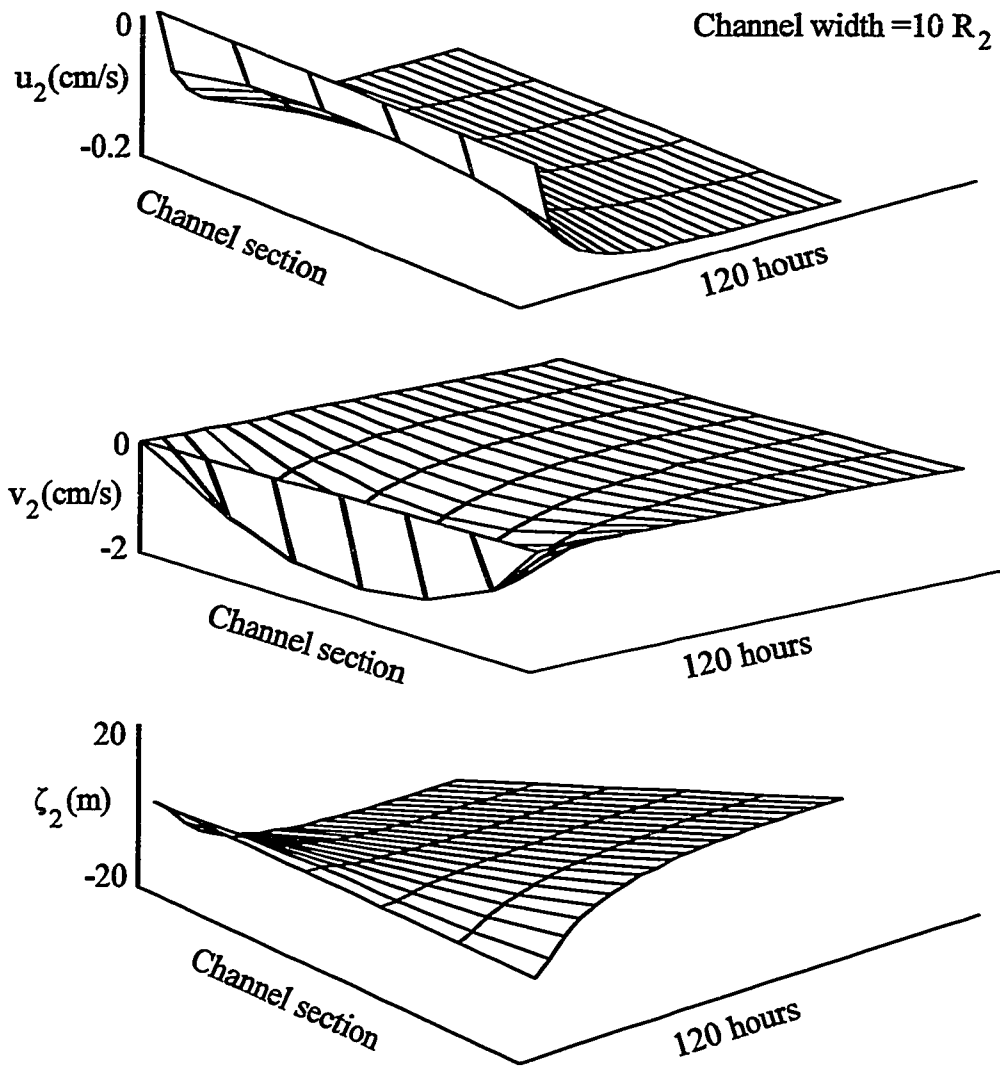


Figure 3.5: Space-time distributions of the channel flow lower layer components for a channel width of $10R_2$ (150 km).

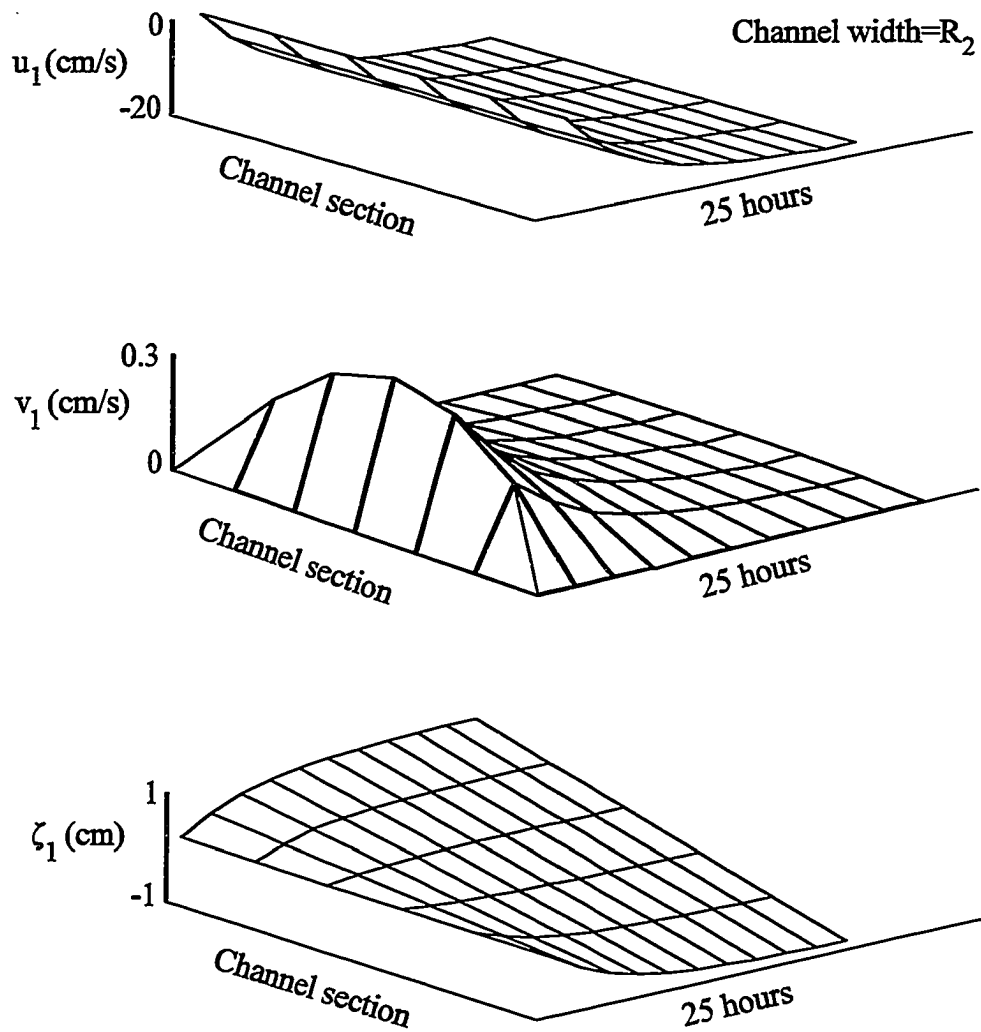


Figure 3.6: Space-time distributions of the channel flow lower layer components for a channel width of R_2 (15 km).

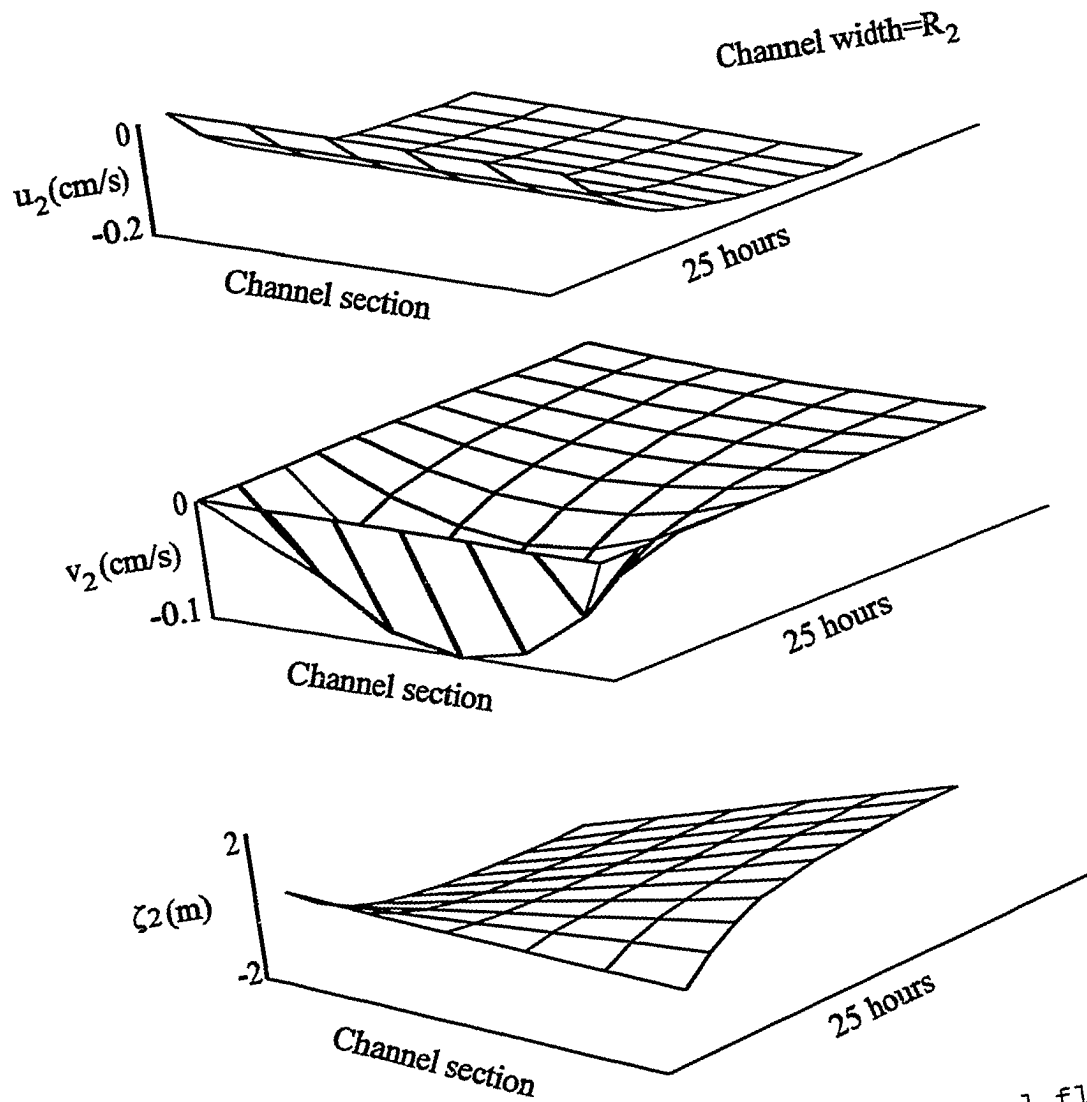


Figure 3.7: Space-time distributions of the channel flow lower layer components for a channel width of R_2 (15 km).

survive even under continued wind forcing.

The implications of this model are important. The characteristic time scales of wind-driven flow in a channel depend not only on the frictional dissipation, but also on distance from shore and thus on the overall channel width. A wide strait will reach steady state much later than a narrow strait.

The strait of Gibraltar is a paradigm for narrow straits. Its width is nearly equal to the internal Rossby radius of deformation. As such, it will come to steady state quite rapidly. Our results suggests that this process will take on the order of a day. This theoretical result suggests that uniform (in time and cross-channel direction) flow will quickly evolve, and that a single mooring is sufficient to accurately examine the statistical and dynamical relation of winds to strait currents.

However, the Strait bathymetry and coastal configuration do not satisfy the restraining hypotheses used in the proposed model. One way to address the adjustment over bathymetry is to introduce a coastal shelf within the upper layer as shown below:

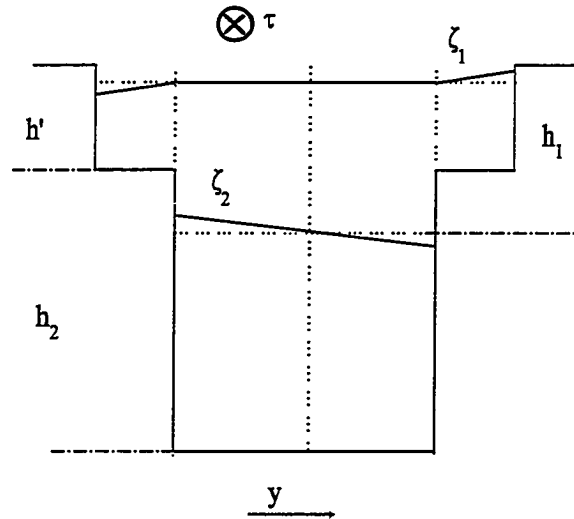


Figure 3.9: Two-layer schematic cross-section for the adjustment over bathymetry.

Within these relatively small portions of the channel cross section, the flow is described by a one-layer set of equations forced by the wind stress. The resulting steady flow (primed variables) is again reduced to a slablike structure, controlled by the bottom stress only:

$$\left\{ \begin{array}{l} \overline{u'}(y) = \frac{1}{Cb} \frac{\tau}{\rho_1 h'} \\ \overline{v'}(y) = 0 \\ \overline{\zeta'}(y) = -\frac{f}{g} \frac{1}{Cb} \frac{\tau}{\rho_1 h'} y \end{array} \right.$$

The cross-channel flows in either side have vanished due to the coastal boundary constraints. Compared to the steady state solution of the two-layer region, this solution is controlled only by the step depth h' since $C_i \ll C_b$. For a bathymetry configuration as steep as that of Gibraltar Strait, the depth h' can be estimated as approximately 40 m for an average shelf width of 500 m. The ratio of shelf velocity to the center channel velocity is:

$$\frac{\overline{u'}(y)}{\overline{u_1}(y)} = \frac{C_b}{C_b + C_i} \frac{h'}{h_1} \approx \frac{h'}{h_1}$$

Thus, the current is 2.5 times stronger in these locations than in the middle of the cross-channel section, which accentuates the coastally trapped flow. The seasurface distribution at these two shelf regions being in geostrophic equilibrium with the flow, also have slopes h'/h_1 (in this case 2.5) times steeper than the seasurface slope in the center region of the Strait.

Conclusions

Statistical analysis of meteorological and current-meter data shows clearly that, within the subtidal frequency range, wind and atmospheric pressure, taken as uncorrelated forcings, contribute a similar percentage to the current variance in the Strait of Gibraltar. This result is the first statistical demonstration of wind-driving in the Strait. The larger portion of the wind stress, that correlated to atmospheric pressure differences, may also be expected to directly force currents through the Strait. However, with the data available it is not possible to statistically discriminate between the correlated wind stress and atmospheric pressure forcing functions.

The inviscid channel jet model assumes an idealized long straight channel of rectangular cross section. Despite its restrictive hypotheses, the model's analytic solution permits great insight into the wind-forced flow dynamics. The model deals explicitly with the initiation of upwelling and downwelling of the pycnocline, and geostrophic adjustment of a two layer fluid in response to the wind forcing parallel to the channel walls. Although its validity holds for a rather short time scale, the channel jet solution is explicitly expressed in terms of barotropic and baroclinic fields scaled by internal and external Rossby

radii (R_1 and R_2). This decomposition leads to an understanding of the way momentum is distributed in each layer before the friction terms become too large to be neglected.

In the sense that its width approximately equals the local internal Rossby radius of deformation, R_2 , the Strait of Gibraltar is a prototype of a narrow channel. Although the fundamental nature of the channel jet is coastally trapped, in a narrow channel, cross-channel variations are insignificant. As such the resulting flow structure is slablike, in stark contrast to a channel wide relative to R_2 . Another hallmark of the inviscid channel jet is its linear dependence on time. This feature results in unrealistically large solutions for large values of time, so that the solution is best thought of as valid only for the initiation of the flow.

Of the simplifying assumptions made in the channel jet model, the most restrictive is the neglect of frictional dissipation. Accordingly, linear drag laws representing interface and bottom friction were introduced into the two-layer shallow water equations. A steady state solution of these equations is easily obtained that shows slab flow in the upper and lower layers, with the along-channel current being determined by a direct balance between wind forcing and dissipation. The time dependent frictional model is investigated through a numerical solution using a staggered

space-time grid and the finite difference approximation. This numerical analysis illuminates the process by which the coastally trapped channel jet evolves into the slablike steady state. The numerical solution initially behaves the same as the analytical channel jet solution and is characterized by coastally trapped currents and seasurface and interface displacements that grow with time. After approximately six hours for a channel width of $10R_2$, the effects of dissipation become evident and the acceleration of the current slows. The near shore currents, being greater than those of mid-channel, are the first to achieve the steady state equilibrium between the wind stress forcing and the frictional dissipation. Once the steady state has been reached, there is no cross-channel flow nor change in seasurface and interface displacements. This state occurs successively at locations farther from shore until, in a flat bottom channel, the solution reduces to a two-layer along-channel slab flow, with linear cross-channel tilts of the seasurface and interface.

In summary, the flow field goes through a frictional adjustment to steady state that begins at the coasts and propagates toward center channel. From the perspective of the cross-channel flow, it is as if the channel width was reducing in time.

This study helped us understand how the wind momentum would be distributed over the two layers in the Strait of

Gibraltar. Theoretically, it suggests that, because of the narrowness of the Strait and its short frictional adjustment time scale, a single current-meter mooring placed in the channel is sufficient for the investigation of the wind-driven flow. Currents forced by wind events such as strong Levante, which usually last 3 to 5 days, are predicted to reach the steady state after only one day.

The influence of a non rectangular channel in the Strait can be investigated to zero order by introducing flat bottom shallow flanks to the channel upper layer. The steady state solution shows that the flanks intensify the current with respect to the current in the main channel. This result is consistent with anecdotal accounts of wind-driven currents on the shallow flanks flowing against the Atlantic inflow.

Some insight into the importance of the long straight channel assumption used throughout this work is provided by a numerical study by Crépon et al. (1984). The study showed that changes in coastline orientation generate barotropic and baroclinic waves that tend to "shut down" the developing coastal jets. Because of the speed with which the barotropic waves travel, the barotropic response in the Strait of Gibraltar could be quickly suppressed. On the other hand the baroclinic jet may be expected to show significant effect of along channel geometry on a time scale of the same order as

the frictional adjustment time (~1 day).

Although the models presented in this thesis rely on several assumption that are imperfect approximations, these shortcoming affect the quantitative rather than the qualitative behavior of wind-driven flow in the Strait. Conclusive corroboration of the dynamical predictions of models could be provided in a future experiment by deploying three bottom-mounted DAPCMs across the Strait at locations that would provide detailed data in both the Atlantic and Mediterranean layers. By this design the separation of responses to wind and pressure difference forcing may be achievable.

In order to verify the time behavior of the wind-driven channel flow, one needs a long channel with a local internal Rossby radius much smaller than the channel width. A quick review of the world straits reveals that some channels could satisfy these criteria. Among them the Hudson Strait seems most suitable since it has an almost flat bottom 1000 m deep, and long (1500 km) straight coasts. The channel width of roughly 500 km is nearly two orders of magnitude greater than the internal Rossby radius. During fall and summer wind events, before the ice forms at the surface, stratification is so dramatic (Tomczak et al., 1994) that the water column could be grossly discretized in two layers. Each channel configuration has its own limitations and an extensive numerical investigation is still the technique of choice to

investigate the wind-driven flow through a two-layer channel.

REFERENCES

- Bendat J.S., 1976. Solutions For The Multiple Input/Output Problem, *Journal of Sound And Vibration*, 44(3), 311-325.
- Bendat J.S. and A.G. Piersol, 1980. *Engineering Applications of Correlation and Spectral Analysis*. Wiley-Interscience Publication, John Wiley & Sons ed., New York.
- Bendat J.S. and A.G. Piersol, 1986. *Random Data Analysis and Measurement Procedures*, 2nd ed., Wiley-Interscience Publication, John Wiley & Sons ed., New York.
- Bethoux J.P., 1979. Budgets of the Mediterranean Sea. Their dependence on the local climate and on the characteristics of the Atlantic waters, *Oceanologica Acta*, 2, 157-163.
- Bethoux J.P., 1980. Mean water fluxes across sections in the Mediterranean Sea, evaluated on the basis of water and salt budgets and of observed salinities, *Oceanologica Acta*, 3, 76-88.
- Bormans M.C., C. Garrett and K.R. Thompson, 1986. Seasonal variability of the surface inflow through the Strait of Gibraltar, *Oceanologica Acta*, 9, 403-414.
- Bormans M.C. and C. Garrett, 1989. The Effects of Non-rectangular Cross Section, Friction, and Barotropic Fluctuations on the exchange through the Strait of Gibraltar, *Journal of Physical Oceanography*, 19, 1543-1557.
- Bryden H.L. and T.H. Kinder, 1988. Gibraltar Experiment: a plan for dynamic and kinematic investigations of strait mixing, exchange and turbulence, *Oceanologica Acta*, 9, 29-40.
- Bryden H.L. and H.M. Stommel, 1984. Limiting processes that determine basic features of the circulation in the Mediterranean Sea, *Oceanologica Acta*, 7, 289-296.
- Candela J., 1989. *Tidal and Subinertial Flows through the Strait of Gibraltar*, PhD Dissertation, University of California at San Diego.

Candela J., C.D. Winant and H.L. Bryden, 1989. Meteorologically forced subinertial flows through the Strait of Gibraltar, *Journal of Geophysical Research*, 94(C9), 12667-12679.

Conrado A.R.C. and A.J. Clarke, 1987. Interaction of Ocean Tides through a Narrow Single Strait and Narrow Multiple Straits, *Journal of Physical Oceanography*, 17, 2203-2218.

Crépon M., 1965. Influence de la pression atmosphérique sur le niveau moyen de la Méditerranée occidentale et sur le niveau moyen à travers le Déroit de Gibraltar, *Cahiers Océanographiques*, 1(7), 15-32.

Crépon M., 1971. Hydrodynamique marine en régime impulsional, Thèse de Doctorat d'Etat es Sciences Physiques, Faculté des Sciences de Paris, France.

Crépon M. and C. Richez, 1982. Transient upwelling generated by two-dimensional atmospheric forcing and variability in the coastline, *Journal of Physical Oceanography*, 12, 1437-1457.

Crépon M., C. Richez and M. Chartier, 1984. Effects of Coastline Geometry on Upwellings, *Journal of Physical Oceanography*, 14, 1365-1382.

Csanady G.T., 1977. The coastal jet conceptual model in the dynamics of shallow seas, in *The Sea*, vol. 6, edited by E.D. Goldberg, I.N. McCave, J.J. O'Brien, and J.H. Steele, 117-144, John Wiley, New York.

Csanady G.T., 1982. *Circulation in the Coastal Ocean*, D. Reidel Publishing Company, Dordrecht Holland.

Dorman C.E., 1988. Meteorological observations in the Strait of Gibraltar, contributed presentation in: *Gibraltar Experiment*, T.H. Kinder and H.L. Bryden, Woods Hole Oceanographic Institution Technical Report, WHOI-88-30.

Garrett C.J.R., 1983. Variable sea level and strait flows in the Mediterranean: a theoretical study of the response to meteorological forcing, *Oceanologica Acta*, 6(1), 79-87.

Garrett C.J.R. and F. Majaess, 1984. Nonisostatic Response of Sea Level to Atmospheric Pressure in the Eastern Mediterranean, *Journal of Physical Oceanography*, 14, 656-665.

Gill A.E., 1982. *Atmosphere-Ocean Dynamics*. International Geophysics Series, Volume 30, Academic Press, New York.

Gilbert Denis, 1990. Theory and observations of internal wave reflection off sloping topography, PhD Dissertation, Dalhousie University.

Greenspan D., 1974. Discrete Numerical Methods in Physics and Engineering, V 107, Mathematics in Science and Engineering.

Jenter H.L. and O.S. Madsen, 1989. Bottom stress in wind-driven depth-averaged coastal flows, Journal of Physical Oceanography, 19, 962-974.

Kundu P.K., J.S. Allen and R.L. Smith, 1975. Modal Decomposition of the Velocity Field near the Oregon Coast, Journal of Physical Oceanography, 5, 683-704.

Lacombe H. and C. Richez, 1982. The regime of the Strait of Gibraltar. In: Hydrodynamics of Semi-Enclosed Seas, J.C.J. Nihoul ed., Elsevier, Amsterdam, 13-74.

Nuttall A.H., 1971. Spectral Estimation by Means of Overlapped Fast Fourier Transform Processing of Windowed Data, Naval Underwater Systems Center Report 4169.

Pettigrew N.R., 1981. The dynamics and Kinematics of the coastal boundary layer off Long Island. PhD Dissertation Joint Program MIT/WHOI.

Pettigrew N.R. and S.P. Murray, 1986. The coastal boundary layer and inner shelf. Baroclinic Processes on Continental Shelves, Coastal and Estuarine Sciences 3, American Geophysical Union, 95-108.

Pettigrew N.R. and R.A. Hyde, 1989. The structure of the internal bore in the Strait of Gibraltar and its influence on the Atlantic inflow, NATO Advanced Topics Workshop on Strait Dynamics, Les Arcs, France.

Poon Y.K. and O.S. Madsen, 1991. A Two-Layer Wind Driven Coastal Circulation Model, Journal of Geophysical Research, 96(C2), 2535-2548.

Stanton B.R., 1983. Low frequency variability in the Mediterranean outflow west of Gibraltar, Deep-Sea Research, 30, 743-761.

Tomczak M. and J.S. Godfrey, 1994. Regional Oceanography: an introduction. Pergamon Press, Elsevier Science Ltd.

Wu J., 1980. Wind-stress coefficients over sea surface near neutral conditions: a revisit, Journal of Physical Oceanography, 10, 727-740.

Wu J., 1982. Wind-stress coefficients over sea surface from breeze to Hurricane, Journal of Geophysical Research, 87(C12), 9704-9706.

APPENDIX 1

Empirical Orthogonal Functions in time domain applied to complex current time series

Considering a profile of N current time series, the well known EOF analysis deals with one component at a time and provides covarying modes. Here, to couple the vector components in the modal analysis and avoid separate analysis for each component of the current, an Empirical Orthogonal Function Analysis program EOFTIME was developed for complex velocity inputs.

Each horizontal velocity vector of two time series $[u_j(t), v_j(t)]$ is interpreted as a scalar time series $X_j(t) = u_j(t) + iv_j(t)$, where i is the pure imaginary unit. EOFTIME integrates up to 30 complex inputs.

At first, a simple routine retains only the time overlapping part of each complex time series such as all time series used are based on the same time range $t=1,2,3\dots N$. Then the zero temporal lag cross-covariance matrix A is constructed from time series X_j and X_k according to:

$$A_{jk} = \frac{1}{N} \sum_{t=1}^N \{X_j(t) - \bar{X}_j\} \{X_k^*(t) - \bar{X}_k^*\}$$

where the star upper index and the overbar operators denote respectively the complex conjugate and the mean value. The matrix A is Hermitian, i.e.:

$$A_{jk} = \overline{A_{kj}}$$

and as such, its diagonal is real.

The objective is to diagonalize A, then to express its eigen vectors in a normalized form. The diagonalization is performed through the use of a IMSL subroutine DEVCSF. The eigen couples (λ_j, e_{jk}) are composed of real eigen values and orthogonal vectors and satisfy the relation:

$$\sum_{l=1}^N A_{lk} e_{jl} = \lambda_j e_{jk}$$

The eigen value λ_j designates the percentage of total variance carried by the associated mode which representant is the eigen vector e_{jk} .

Expanding the data in this empirical orthogonal modes leads to:

$$c_j(t) = \sum_{k=1}^N a_k(t) e_{kj}$$

where the complex amplitude time series $a_k(t)$ is the k-th

eigen function:

$$a_k(t) = \sum_{j=1}^N e_{kj}^* c_j(t)$$

EOFTIME provides the N complex amplitudes $a_k(t)$ and the corresponding normalized eigen functions e'_{kj} computed as:

$$e'_{kj} = \sqrt{\lambda_k} e_{kj}$$

These normalized functions play the role of weight functions for the associated mode. The actual j -mode time series $U_{m,j}(t)$ and $V_{m,j}(t)$ are derived as real and imaginary part of the complex time series:

$$X_{m,j}(t) = \sum_{k=1}^N e_{jk} X_j(t)$$

APPENDIX 2

Partial and Multiple Coherences (Bendat and Piersol, 1971,1980)

A system involving a single output forced by two correlated inputs is considered (Figure 1):

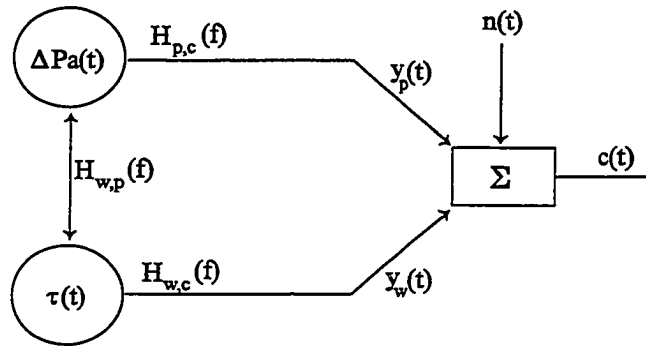


Figure 1: Correlated two-input/one-output model

where:

$\tau(t)$ [$T(f)$] , $\Delta Pa(t)$ [$\Pi(f)$] and $n(t)$ [$N(f)$] are respectively the correlated input signals and the system noise in time domain and their corresponding bracketed Fast Fourier Transforms (FFT),

$H_{p,c}(f)$, $H_{w,p}(f)$ and $H_{w,c}(f)$ are the response functions,

$y_w(t)$ and $y_p(t)$ mark the output signals of $H_{w,c}(f)$ and $H_{p,c}(f)$,

$c(t)$ [$C(f)$] is the output signal of the system and its

FFT.

This system assumes the noise signal non correlated to the inputs cited, and all inputs random records.

This design is based on a constant parameter linear system:

$$c(t) = y_w(t) + y_p(t) + n(t)$$

The FFT of this equation translates to:

$$C(f) = H_{w,c}(f) T(f) + H_{p,c}(f) \Pi(f) + N(f)$$

Using the definition of the cross spectrum of two signals, the response functions $H_{w,c}(f)$ and $H_{p,c}(f)$ are expressed as:

$$H_{w,c}(f) = \frac{G_{w,c}(f)}{G_{w,w}(f)} \frac{1 - \frac{G_{w,p}(f) G_{p,c}(f)}{G_{p,p}(f) G_{w,c}(f)}}{1 - \gamma_{w,p}^2}$$

$$H_{p,c}(f) = \frac{G_{p,c}(f)}{G_{p,p}(f)} \frac{1 - \frac{G_{p,w}(f) G_{w,c}(f)}{G_{w,w}(f) G_{p,c}(f)}}{1 - \gamma_{w,p}^2}$$

where any set of signals $\{x(t), y(t)\}$ produces the spectrum $G_{x,y}(f) = X^*(f) Y(f)$ and the ordinary coherence:

$$Y_{x,y}^2(f) = \frac{|G_{x,y}(f)|^2}{G_{x,x}(f) G_{y,y}(f)}$$

Partail coherences

Let's consider the conditioned signals $\tau_{w/p}(t)$ and $\tau_{w:p}(t)$ derived from the single input/single output system (Figure 2):

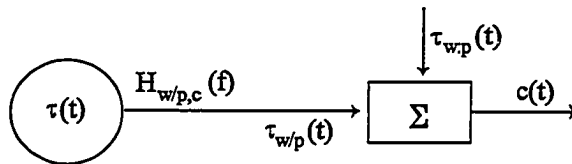


Figure 2: Decomposition of the wind input

the subsequent response function being:

$$H_{p,c}(f) = \frac{G_{p,c}(f)}{G_{p,p}(f)}$$

Now the wind signal is divided in a pressure correlated part $\tau_{w:p}(t)$ and a totally uncorrelated signal noted $\tau_{w/p}(t)$:

$$\tau(t) = \tau_{w:p}(t) + \tau_{w/p}(t)$$

This equation becomes in frequency domain:

$$T(f) = H_{p,w}(f) \Pi(f) + T_{w/p}(f)$$

Similarly, the auto spectrum of the wind signal is decomposed in:

$$G_{w,w}(f) = G_{w,w:p}(f) + G_{w,w/p}(f)$$

This decomposition leads to a "2 uncorrelated inputs/single output" system (Figure 3):

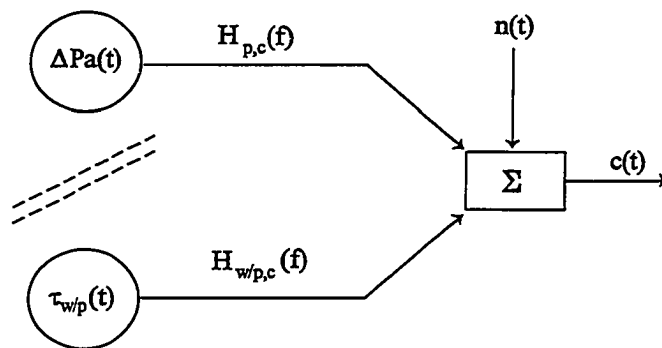


Figure 3: Uncorrelated two-input/one output model

Thus the FFT of the current becomes:

$$C(f) = H_{p,c}(f) \Pi(f) + H_{w,c}(f) T_{w/p}(f) + N(f)$$

Consequently, new spectra terms arise:

$$G_{w/p,c}(f) = G_{w,c}(f) - \frac{G_{w,p}(f)}{G_{p,p}(f)} G_{p,p}(f)$$

$$G_{w/p,w}(f) = (1 - \gamma_{p,w}^2(f)) G_{w,w}(f)$$

$$G_{c/p,c}(f) = (1 - \gamma_{p,c}^2(f)) G_{c,c}(f)$$

leading to the partial coherences:

$$\gamma_{p/w,c}^2(f) = \frac{|G_{p/w,c}(f)|^2}{G_{p/w,p}(f) G_{c/w,c}(f)}$$

$$\gamma_{w/p,c}^2(f) = \frac{|G_{w/p,c}(f)|^2}{G_{w/p,w}(f) G_{c/p,c}(f)}$$

Multiple coherence

In our case, a multiple coherence concerns the fractional portion of the current auto spectrum due to the inputs as a whole. Since:

$$C(f) = H_{w,c}(f) T(f) + H_{p,c}(f) \Pi(f) + N(f)$$

and the current auto spectrum formula $G_{c,c}(f) = C^*(f) C(f)$,
it becomes:

$$\begin{aligned} G_{c,c}(f) = & \left\{ |H_{w,c}(f)|^2 G_{w,w}(f) \right. \\ & + H_{w,c}^*(f) H_{p,c}(f) G_{w,p}(f) + H_{p,c}^*(f) H_{w,c}(f) G_{p,w}(f) \\ & \left. + |H_{p,c}(f)|^2 G_{p,p}(f) \right\} + G_{n,n}(f) \end{aligned}$$

The right terms are written with respect to the noise input, i.e. the term between brackets deals only with spectral quantities derived from the inputs while the second term is a current-noise only spectrum. Following the same notation as for the partial coherences, the current autospectrum can be expressed as:

$$G_{c,c}(f) = G_{c:i,c}(f) + G_{c:n,c}(f)$$

where the indexes i and n stand for inputs and noise signals.

Ultimately, the multiple coherence definition is:

$$Y_{c:i,c}^2(f) = \frac{G_{c:i,c}(f)}{G_{c,c}(f)} = 1 - \frac{G_{c:n,c}(f)}{G_{c,c}(f)}$$